

1 **Technical note: Applicability of physics-based and machine-learning-based**  
2 **algorithms of geostationary satellite in retrieving the diurnal cycle of cloud base**  
3 **height**

4

5 Mengyuan Wang<sup>1</sup>, Min Min<sup>1\*</sup>, Jun Li<sup>2</sup>, Han Lin<sup>3</sup>, Yongen Liang<sup>1</sup>, Binlong Chen<sup>2</sup>,  
6 Zhigang Yao<sup>4</sup>, Na Xu<sup>2</sup>, Miao Zhang<sup>2</sup>

7

8

9 <sup>1</sup>School of Atmospheric Sciences, Southern Marine Science and Engineering  
10 Guangdong Laboratory (Zhuhai), and Guangdong Province Key Laboratory for  
11 Climate Change and Natural Disaster Studies, Zhuhai 519082, China

12 <sup>2</sup>Key Laboratory of Radiometric Calibration and Validation for Environmental  
13 Satellites and Innovation Center for FengYun Meteorological Satellite (FYSIC),  
14 National Satellite Meteorological Center (National Center for Space Weather), China  
15 Meteorological Administration, Beijing 100081, China

16 <sup>3</sup>Key Laboratory of Spatial Data Mining and Information Sharing of Ministry of  
17 Education, National and Local Joint Engineering Research Center of Satellite  
18 Geospatial Information Technology, Fuzhou University, Fuzhou 350108, China

19 <sup>4</sup>Beijing Institute of Applied Meteorology, Beijing 100029, China

20

21

22

23 *Correspondence to:* Min Min (minm5@mail.sysu.edu.cn)

24

25

26

27

28

29

30

31

32

33

34 **Abstract.** Two groups of retrieval algorithms, physics-based and the other  
35 machine-learning (ML) based, each consisting of two independent approaches, have  
36 been developed to retrieve cloud base height (CBH) and its diurnal cycle from  
37 Himawari-8 geostationary satellite observations. Validations have been conducted  
38 using the joint CloudSat/CALIOP (Cloud-Aerosol Lidar with Orthogonal Polarization)  
39 CBH products in 2017, ensuring independent assessments. Results show that the two  
40 ML-based algorithms exhibit markedly superior performance (the optimal method is  
41 with a correlation coefficient of  $R > 0.91$  and an absolute bias of approximately 0.8  
42 km) compared to the two physics-based algorithms. However, validations based on  
43 CBH data from the ground-based lidar at the Lijiang station in Yunnan province and  
44 the cloud radar at the Nanjiao station in Beijing, China, explicitly present  
45 contradictory outcomes ( $R < 0.60$ ). An identifiable issue arises with significant  
46 underestimations in the retrieved CBH by both ML-based algorithms, leading to an  
47 inability to capture the diurnal cycle characteristics of CBH. The strong consistence  
48 observed between CBH derived from ML-based algorithms and the spaceborne active  
49 sensors of CloudSat/CALIOP may be attributed to utilizing the same dataset for  
50 training and validation, sourced from the CloudSat/CALIOP products. In contrast, the  
51 CBH derived from the optimal physics-based algorithm demonstrates the good  
52 agreement in diurnal variations of CBH with ground-based lidar/cloud radar  
53 observations during the daytime (with an  $R$  value of approximately 0.7). Therefore,  
54 the findings in this investigation from ground-based observations advocate for the  
55 more reliable and adaptable nature of physics-based algorithms in retrieving CBH  
56 from geostationary satellite measurements. Nevertheless, under ideal conditions, with  
57 an ample dataset of spaceborne cloud profiling radar observations encompassing the  
58 entire day for training purposes, the ML-based algorithms may hold promise in still  
59 delivering accurate CBH outputs.

60 **Key words:** Geostationary meteorological satellite; cloud base height; physics-based  
61 algorithm; machine learning.

62

## 63 1 Introduction

64 Clouds, comprising visible aggregates like atmospheric water droplets,  
65 supercooled water droplets, ice crystals, etc., cover roughly 70% of the Earth's surface  
66 (Stubenrauch et al., 2013). They play a pivotal role in global climate change, the  
67 hydrometeor cycle, aviation safety, and serve as a primary focus in weather  
68 forecasting and climate research, particularly storm clouds (Hansen, 2007; Hartmann  
69 and Larson, 2002). From advanced geostationary (GEO) and polar-orbiting (LEO,  
70 low earth orbit) satellite imagers, various measurable cloud properties, such as cloud  
71 fraction, cloud phase, cloud top height (CTH), and cloud optical thickness ( $D_{\text{COT}}$ ), are  
72 routinely retrieved. However, the high-quality cloud geometric height (CGH) and  
73 cloud base height (CBH), a fundamental macro physical parameter delineating the  
74 vertical distribution of clouds, remains relatively understudied and underreported.  
75 Nonetheless, for boundary-layer clouds, the cloud base height stands as a critical  
76 parameter depending on other cloud-controlling variables. These variables encompass  
77 the cloud base temperature (Zhu et al., 2014), cloud base vertical velocity (Zheng et  
78 al., 2020), activation of CCN (Cloud Condensation Nuclei) at the cloud base  
79 (Rosenfeld et al., 2016; Miller et al., 2023), and the cloud-surface decoupling state  
80 (Su et al., 2022). These factors significantly impact convective cloud development  
81 and ultimately the climate.

82 There are distinct diurnal cycle characteristics of clouds in different regions  
83 across the globe (Li et al., 2022). These diurnal cycle characteristics primarily stem  
84 from the daily solar energy cycle absorbed by both the atmosphere and Earth's surface.  
85 Besides, vertical atmospheric motions are shaped by imbalances in atmospheric  
86 heating and surface configurations, also leading to a range of cloud movements and  
87 structures (Miller et al., 2018). Cloud base plays a pivotal role in weather and climate  
88 processes. It is critical for predicting fog and cloud-related visibility issues important  
89 in aviation and weather forecasting. For instance, lower cloud bases often lead to  
90 more intense rainfall. In climate modeling, CBH is integral for accurate long-term  
91 weather predictions and understanding the radiative balance of the Earth, which  
92 influences global temperatures (Zheng and Rosenfeld, 2015). Hence, the accurate  
93 determination of CBH and its diurnal cycle with high spatiotemporal resolution  
94 becomes very important, necessitating comprehensive investigations (Viúdez-Mora et

删除了: As well known, t

96 al., 2015; Wang et al., 2020). Such efforts can provide deeper insights into potential  
97 ramifications of clouds on radiation equilibrium and global climate systems.

98 However, as one of the most crucial cloud physical parameters in atmospheric  
99 physics, the CBH poses challenges in terms of measurement or estimation from space.  
100 Presently, the primary methods for measuring CBH rely on ground-based  
101 observations, utilizing tools such as sounding balloons, Mie-scattering lidars,  
102 stereo-imaging cloud-height detection technologies, and cloud probe sensors  
103 (Forsythe et al., 2000; Hirsch et al., 2011; Seaman et al., 2017; Zhang et al., 2018;  
104 Zhou et al., 2019; Zhou et al., 2024). While *in-situ* ground-based observation methods  
105 offer highly accurate, reliable, and timely continuous CBH results, they are  
106 constrained by localized observation coverage and the sparse distribution of  
107 observation sites (Aydin and Singh, 2004). In recent decades, with the rapid  
108 advancement of meteorological satellite observation technology, spaceborne  
109 observing methods have emerged that provide global cloud observations with high  
110 spatiotemporal resolution compared to conventional ground-based remote sensing  
111 methods. In this realm, satellite remote sensing techniques for measuring CBH fall  
112 primarily into two categories: active and passive methods. Advanced active remote  
113 sensing technologies like CloudSat (Stephens et al., 2002) and Cloud-Aerosol Lidar  
114 and Infrared Pathfinder Satellite Observation (CALIPSO) (Winker et al., 2009) in the  
115 National Aeronautics and Space Administration (NASA) A-Train (Afternoon-Train)  
116 series (Stephens et al., 2002) can capture global cloud profiles, including CBH, with  
117 high quality by detecting unique return signals from cloud layers using onboard active  
118 millimeter wave radar or lidar. However, their viewing footprints are limited along the  
119 nadir of the orbit, implying that observation coverage remains confined primarily to a  
120 horizontal scale (Min et al., 2022; Lu et al., 2021).

121 In addition to active remote sensing methods, satellite-based passive remote  
122 sensing technologies can also play an important role in estimating CBH (Meerkötter  
123 and Bugliaro, 2009; Lu et al., 2021). The physics-based principles and retrieval  
124 methods for CTH have reached maturity and are now widely employed in satellite  
125 passive remote sensing field (Heidinger and Pavolonis, 2009; Wang et al., 2022).  
126 However, the corresponding physical principles or methods for measuring CBH using  
127 satellite passive imager measurements are still not entirely clear and unified  
128 (Heidinger et al., 2019; Min et al., 2020). A recent study by Yang et al. (2021) utilized  
129 oxygen A-band data observed by the Orbiting Carbon Observatory 2 (OCO-2) to

删除了:(

删除了:,

132 retrieve single-layer marine liquid CBH. These passive space-based remote sensing  
133 methods aforementioned, such as satellite imagery, play a key role in retrieving CBH.  
134 In terms of detection principles, the first method involves the extrapolation technique  
135 for retrieving CBH for clouds of the same type. For instance, Wang et al. (2012)  
136 proposed a method to extrapolate CBH from CloudSat using spatiotemporally  
137 matched MODIS (Moderate Resolution Imaging Spectroradiometer) cloud  
138 classification data (Baum et al., 2012; Platnick et al., 2017). The second  
139 physics-based retrieval method first approximates the cloud geometric thickness using  
140 its optical thickness. It then employs the previously derived CTH product to compute  
141 the corresponding CBH using the respective NOAA (National Oceanic and  
142 Atmospheric Administration) SNPP/VIIRS (Suomi National Polar-orbiting  
143 Partnership/Visible Infrared Imaging Radiometer Suite) products (Noh et al., 2017).  
144 Hutchison et al. (2002 and 2006) also formulated an empirical algorithm that  
145 estimates both cloud geometric thickness (CGT) and CBH. This algorithm relies on  
146 statistical analyses derived from MODIS  $D_{COT}$  and cloud liquid water path products  
147 (Hutchison et al., 2006; Hutchison, 2002).

148 Machine learning (ML) has proven to be highly effective in addressing nonlinear  
149 problems within remote sensing and meteorology fields, such as precipitation  
150 estimation and CTH retrieval (Min et al., 2020; HåKansson et al., 2018; Kühnlein et  
151 al., 2014). In recent years, several studies have leveraged ML-based algorithms to  
152 retrieve CBH, establishing nonlinear connections between CBH and GEO satellite  
153 observations. For instance, Tan et al. (2020) integrated CTH and cloud optical  
154 properties products from Fengyun-4A (FY-4A) GEO satellite with spatiotemporally  
155 matched CBH data from CALIPSO/CloudSat. They developed a random forest (RF)  
156 model for CBH retrieval. Similarly, Lin et al. (2022) constructed a gradient boosted  
157 regression tree (GBRT) model using U.S. new-generation Geostationary Operational  
158 Environmental Satellites-R Series (GOES-R) Advanced Baseline Imager (ABI) level  
159 1B radiance data and the ERA5 (the fifth generation ECMWF) reanalysis dataset (Lin  
160 et al., 2022) (<https://cds.climate.copernicus.eu/cdsapp#!/search?type=dataset>). They  
161 employed CALIPSO CBH data as labels to achieve single-layer CBH retrievals.  
162 Notably, the CBH quality of ML-based algorithms was found to surpass that of  
163 physics-based algorithms (Lin et al., 2022). Moreover, Tana et al. (2023) utilized  
164 Himawari-8 data and the RF algorithm to develop a novel CBH algorithm, achieving  
165 a similar high correlation coefficient (R) of 0.92 and a low root mean square error

删除了:(

删除了:,

168 (RMSE) of 1.17 km compared with CloudSat/CALISPO data.

169 However, these former studies did not discuss whether both physics-based and  
170 ML-based algorithms of GEO satellite could retrieve the diurnal cycle of CBH well.  
171 This gap in research could be mainly attributed to potential influences from the fixed  
172 LEO satellite (with active radar or lidar) passing time in the previous CBH retrieval  
173 model (Lin et al., 2022). The diurnal cycles of CBH have not been well investigated  
174 in both GEO and LEO remote sensing research. Hence, it is crucial to thoroughly  
175 investigate the diurnal cycle features of CBH derived from GEO satellite  
176 measurements by comparing them with ground-based radar and lidar observations  
177 (Min and Zhang, 2014; Warren and Eastman, 2014). In this study, we aim to assess  
178 the applicability and feasibility of both physics-based and ML-based algorithms of  
179 GEO satellites in capturing the diurnal cycle characteristics of CBH.

180 The subsequent sections of this paper are structured as follows. Section 2  
181 provides a concise overview of the data employed in this study. Following that,  
182 section 3 introduces the four distinct physics/ML-based CBH retrieval algorithms. In  
183 section 4, the CBH results obtained from these four algorithms are analyzed, and  
184 comparisons are drawn with spatiotemporally matched CBHs from ground-based  
185 cloud radar and lidar. Finally, section 5 encapsulates the primary conclusions and new  
186 findings derived from this study.

## 187 **2 Data**

188 In this study, observations from the Himawari-8 (H8) Advanced Himawari  
189 Imager (AHI) are utilized for the retrieval of high spatiotemporal resolution CBH.  
190 Launched successfully by the Japan Meteorological Administration on October 7,  
191 2014, the H8 geostationary satellite is positioned at 140.7°E. The AHI onboard H8  
192 encompasses 16 spectral bands ranging from 0.47  $\mu\text{m}$  to 13.3  $\mu\text{m}$ , featuring spatial  
193 resolutions of 0.5–2 km. This includes 3 visible (VIS) bands at 0.5–1 km, 3  
194 near-infrared (NIR) bands at 1–2 km, and 10 infrared (IR) bands at 2 km. The  
195 H8/AHI can scan a full disk area within 10 minutes, two specific areas within 2.5  
196 minutes, a designated area within 2.5 minutes, and two landmark areas within 0.5  
197 minutes (Iwabuchi et al., 2018). Its enhanced temporal resolution and observation  
198 frequency facilitate the tracking of rapidly changing weather systems, enabling the  
199 accurate determination of quantitative atmospheric parameters (Bessho et al., 2016).

200 Operational H8/AHI Level-1B data, accessible from July 7, 2015, are freely  
201 available on the satellite product homepage of the Japan Aerospace Exploration  
202 Agency (Letu et al., 2019). The Level-2 cloud products utilized in this study,  
203 including cloud mask (CLM), CTH, cloud effective particle radius (CER or  $R_{\text{eff}}$ ), and  
204  $D_{\text{COT}}$ , are generated by the Fengyun satellite science product algorithm testbed  
205 (FYGAT) (Wang et al., 2019; Min et al., 2017) of the China Meteorological  
206 Administration (CMA) for various applications. According to previous CALIPSO  
207 validations (Min et al., 2020), the absolute bias of cloud top height retrieved by the  
208 H8 satellite is approximately 3 km, with an absolute bias of 1 to 2 km for samples  
209 below 5 km. The accuracy of CTH is crucial for estimating CBH in the subsequent  
210 algorithm. It is important to note that certain crucial preliminary cloud products, such  
211 as CLM, have been validated in prior studies (Wang et al., 2019; Liang et al., 2023).  
212 Nevertheless, before initiating CBH retrieval, it is imperative to validate the H8/AHI  
213 cloud optical and microphysical products from the FYGAT retrieval system. This  
214 validation has been carried out by using analogous MODIS Level-2 cloud products as  
215 a reference. Additional details regarding the validation of cloud products are provided  
216 in the Appendix A section.

217 In addition to the H8/AHI Level-1/2 data, the Global Forecast System (GFS)  
218 numerical weather prediction (NWP) data are employed for CBH retrieval in this  
219 study. The variables include land/sea surface temperature and the vertical profiles of  
220 temperature, humidity, and pressure. Operated by the U.S. NOAA (Kalnay et al.,  
221 1996), the GFS serves as a global and advanced NWP system. The operational GFS  
222 system routinely delivers global high-quality and gridded NWP data at 3-hour  
223 intervals, with four different initial forecast times per day (00:00, 06:00, 12:00, and  
224 18:00 UTC). The three-dimensional NWP data cover the Earth in a  $0.5^\circ \times 0.5^\circ$  grid  
225 interval and resolve the atmosphere with 26 vertical levels from the surface (1000 hPa)  
226 up to the top of the atmosphere (10 hPa).

227 As previously mentioned, the official MODIS Collection-6.1 Level-2 cloud  
228 product Climate Data Records (Platnick et al., 2017) are utilized in this study to  
229 validate the H8/AHI cloud products (CTH, CER, and  $D_{\text{COT}}$ ) generated by the FYGAT  
230 system. High-quality, long-term series MODIS data is often used as a validation  
231 reference to evaluate the products of new satellites. MODIS sensors are onboard  
232 NASA Terra and Aqua polar-orbiting satellites. Terra functions as the morning  
233 satellite, passing through the equator from north to south at approximately 10:30 local

234 time, while Aqua serves as the afternoon satellite, traversing the equator from south to  
235 north at around 13:30 local time. As a successor to the NOAA Advanced Very High  
236 Resolution Radiometer (AVHRR), MODIS features 36 independent spectral bands  
237 and a broad spectral range from 0.4  $\mu\text{m}$  (VIS) to 14.4  $\mu\text{m}$  (IR), with a scanning width  
238 of 2330 km and spatial resolutions ranging from 0.25 to 1.0 km. Recent studies  
239 (Baum et al., 2012; Platnick et al., 2017) have highlighted significant improvements  
240 and collective changes in cloud top, optical, and microphysical properties from  
241 Collection-5 to Collection-6.

242 In addition to the passive spaceborne imaging sensors mentioned above, the  
243 CloudSat satellite, equipped with a 94-GHz active cloud profiling radar (CPR), holds  
244 the distinction of being the first sun-synchronous orbit satellite specifically designed  
245 to observe global cloud vertical structures and properties. It is part of the A-Train  
246 series of satellites, akin to the Aqua satellite, launched and operated by NASA  
247 (Heymsfield et al., 2008). CALIPSO is another polar-orbiting satellite within the  
248 A-Train constellation, sharing an orbit with CloudSat and trailing it by a mere 10–15  
249 seconds. CALIPSO is the first satellite equipped with an active dual-channel CALIOP  
250 at 532 and 1064 nm bands (Hunt et al., 2009). Both CloudSat and CALIPSO possess  
251 notable advantages over passive spaceborne sensors due to the 94-GHz radar of  
252 CloudSat and the joint return signals of lidar and radar on CALIPSO. These features  
253 enhance their sensitivity to optically thin cloud layers and ensure strong penetration  
254 capability, resulting in more accurate CTH and CBH detections compared to passive  
255 spaceborne sensors (CAL\_LID\_L2\_05kmCLay-Standard-V4-10). The joint cloud  
256 type products of 2B-CLDCLASS-LIDAR, derived from both CloudSat and CALIPSO  
257 measurements, offer a comprehensive description of cloud vertical structure  
258 characteristics, cloud type, CTH, CBH, etc. The time interval between each profile in  
259 this product is approximately 3.1 seconds, and the horizontal resolution is 2.5 km  
260 (along track) $\times$ 1.4 km (cross-track). Each profile is divided into 125 layers with a  
261 240-m vertical interval. For more details on 2B-CLDCLASS-LIDAR products, please  
262 refer to the CloudSat official product manual (Sassen and Wang, 2008). In this study,  
263 we consider the lowest effective cloud base height from the joint CloudSat/CALIOP  
264 data as the true values for training and validation. Please note that for this study, we  
265 utilized one-year H8/AHI data and matched it with the joint CloudSat/CALIOP data  
266 from January 1 to December 31 of 2017.



### 267 3 Physics and machine-learning based cloud base height algorithms

#### 268 3.1 GEO cloud base height retrieval algorithm from the interface data processing 269 segment of the Visible Infrared Imaging Radiometer Suite

270 The Joint Polar Satellite System (JPSS) program is a collaborative effort between  
271 NASA and NOAA. The operational CBH retrieval algorithm, part of the 30  
272 Environmental Data Records (EDR) of JPSS, can be implemented operationally  
273 through the Interface Data Processing Segment (IDPS) (Baker, 2011). In this study,  
274 our geostationary satellite CBH retrieval algorithm aligns with the IDPS CBH  
275 algorithm developed by (Baker, 2011). Utilizing the geostationary H8/AHI cloud  
276 products discussed earlier, this new GEO CBH retrieval algorithm is succinctly  
277 outlined below. It is important to note that multilayer cloud scenes remain a challenge  
278 for retrieving both CTH and CBH, especially when considering the column-integrated  
279 cloud water path (CWP) used in physics-based algorithms (Noh et al., 2017). In this  
280 study, we will simplify the scenario by assuming a single-layer cloud for all  
281 algorithms.

282 The new GEO IDPS CBH algorithm initiates the process by first retrieving the  
283 CGT from bottom to top. Subsequently, CGT is subtracted from the corresponding  
284 CTH to calculate CBH ( $CBH = CTH - CGT$ ). The algorithm is divided into two  
285 independent executable modules based on cloud phase, distinguishing between liquid  
286 water and ice clouds. CBH of water cloud retrieval requires  $D_{COT}$  and CER as inputs.  
287 For ice clouds, an empirical equation is employed for CBH retrieval. However, the  
288 standard deviations of error in IDPS CBH for individual granules often exceed the  
289 JPSS VIIRS minimum uncertainty requirement of  $\pm 2$ km (Noh et al., 2017). For a  
290 more comprehensive understanding of this CBH algorithm, please refer to the IDPS  
291 algorithm documentation (Baker, 2011). Note that, similar to previous studies on  
292 cloud retrieval (Noh et al., 2017; Platnick et al., 2017), this investigation also assumes  
293 a single-layer cloud for all CBH algorithms, due to the challenges associated with  
294 determining multilayer cloud structures.

#### 295 3.2 GEO cloud base height retrieval algorithm implemented in the Clouds from 296 Advanced Very High Resolution Radiometer Extended system

297 As mentioned above, the accuracy of the GEO IDPS algorithm is highly  
298 dependent on the initial input parameters such as cloud phase,  $D_{COT}$  and  $R_{eff}$ , which

删除了:/

300 may introduce some uncertainties in the final retrieval results. In contrast, another  
301 statistically-based algorithm is proposed and implemented here, which is named the  
302 GEO CLAVR-x (Clouds from AVHRR Extended, NOAA's operational cloud  
303 processing system for the AVHRR) CBH algorithm (Noh et al., 2017), and it mainly  
304 refers to NOAA AWG CBH algorithm (ACBA) (Noh et al., 2022). Previous studies  
305 have also demonstrated a R of 0.569 and a RMSE of 2.3 km for the JPSS VIIRS  
306 CLAVR-x CBH algorithm. It is anticipated that this algorithm will also be employed  
307 for the NOAA GOES-R geostationary satellite imager (Noh et al., 2017; Seaman et al.,  
308 2017).

309 Similar to the GEO IDPS CBH retrieval algorithm mentioned earlier, the GEO  
310 CLAVR-x CBH retrieval algorithm also initially obtains CGT and CTH, subsequently  
311 calculating CBH by subtracting CGT from CTH (CTH-CGT). However, the specific  
312 calculation method for the CGT value differs. This algorithm is suitable for  
313 single-layer and the topmost layer of multi-layer clouds, computing CBH using the  
314 CTH at the top layer of the cloud. In comparison with the former GEO IDPS CBH  
315 algorithm, the GEO CLAVR-x CBH algorithm considers two additional cloud types:  
316 deep convection clouds and thin cirrus clouds (Baker, 2011). For more details on this  
317 CLAVR-x CBH algorithm, please refer to the original algorithm documentation (Noh  
318 et al., 2017).

### 319 3.3 Random-forest-based cloud base height estimation algorithm

320 RF, one of the most significant ML algorithms, was initially proposed and  
321 developed by (Breiman, 2001). It is widely employed to address classification and  
322 regression problems based on the law of large numbers. The RF method is well-suited  
323 for capturing complex or nonlinear relationships between predictors and predictands.

324 In this study, two distinct ML-based GEO CBH algorithms, namely VIS+IR and  
325 IR-single (only uses observations of H8/AHI IR channels), are devised to retrieve or  
326 predict the CBH using different sets of predictors. The RF training of the chosen  
327 predictors is formulated as follows:

$$328 \text{CBH} = RF_{\text{reg}}[x_1, x_2, \dots, x_n], \quad (1)$$

329 where  $RF_{\text{reg}}$  denotes the regression RF model, and  $x_i$  represents the  $i$ th predictor. The  
330 selected predictors from H8/AHI for both the VIS+IR and IR RF model training and  
331 prediction are detailed in Table 1, mainly referencing Min et al. (2020) and Tan et al.  
332 (2020). The VIS+IR algorithm retrieves CBH using NWP data (atmospheric

333 temperature and altitude profiles, total precipitable water (TPW), surface temperature),  
334 surface elevation, air mass 1 (air mass 1=1/cos(view zenith angle)), and air mass 2 (air  
335 mass 2=1/cos(solar zenith angle)). The rationale for choosing air mass and TPW is  
336 their ability to account for the potential absorption effect of water vapor along the  
337 satellite viewing angle. The predictors in CBH retrieval also include the IR band  
338 Brightness Temperature (BT) and VIS band reflectance. The IR-single algorithm  
339 selects the same GFS NWP data as the VIS+IR algorithm but employs only view  
340 zenith angles and azimuth angles.

341 To optimize the RF prediction model, the hyperparameters of the RF model are  
342 tuned individually. The parameters and their dynamic ranges involved in tuning the  
343 RF prediction models include the number of trees [100, 200, 300, 400, 500], the  
344 maximum depth of trees [10, 20, 30, 40, 50], the minimum number of samples  
345 required to split an internal node [2, 4, 6, 8, 10], and the minimum number of samples  
346 required to be at a leaf node [1, 3, 5, 7, 9]. In this study, we set the smallest number of  
347 trees in the forest to 100 and the maximum depth of the tree to 40.

### 348 3.4 Evaluation method

349 The performance of RF models and physics-based methods will be assessed using  
350 mean absolute error (MAE), mean bias error (MBE), RMSE, R, and standard  
351 deviation (STD) scores using the testing dataset. These scores mentioned above are  
352 used to understand different aspects of the predictive performance of model: MAE  
353 and RMSE provide insights into the average error magnitude, MBE indicates bias in  
354 the predictions, R evaluates the linear association between observed and predicted  
355 values, and STD assesses the variability of the predictions. In the RF IR-single  
356 algorithm, 581,783 matching points are selected from H8/AHI and CloudSat data for  
357 2017. Seventy percent of these points are randomly assigned to the training dataset,  
358 and the remainder serves as the testing dataset. For the RF VIS+IR algorithm, a total  
359 of 418,241 matching points are chosen, with 70% randomly allocated to the training  
360 set. Note that the reduced data amount is because only daytime data can be used for  
361 the VIS+IR method training. It's important to note that the two training datasets in  
362 CloudSat will also be used to verify the CBHs obtained by cloud radar and lidar. The  
363 statistical formulas for evaluation are as follows:

$$364 \text{ MAE} = \frac{1}{n} \sum_{i=1}^n |y_i - x_i|, \quad (2)$$

365  $MBE = \frac{1}{n} \sum_{i=1}^n (y_i - x_i),$  (3)

366  $RMSE = \sqrt{\frac{1}{n} \sum_{i=1}^n (y_i - x_i)^2},$  (4)

367  $R = \frac{\sum_{i=1}^n (y_i - \bar{y})(x_i - \bar{x})}{\sqrt{\sum_{i=1}^n (y_i - \bar{y})^2} \sqrt{\sum_{i=1}^n (x_i - \bar{x})^2}},$  (5)

368  $STD = \sqrt{\frac{1}{n-1} \sum_{i=1}^n (x_i - \bar{x})^2},$  (6)

369 where  $n$  is the sample number,  $y_i$  is the  $i$ th CBH retrieval result, and  $x_i$  is the  $i$ th joint  
370 CloudSat/CALIOP CBH product.

371 Since the two RF models (VIS+IR and IR-single) select 230 typical variables to  
372 fit CBHs, the importance scores of these predictors in the two ML-based algorithms  
373 are ranked for better optimization. In a RF model, feature importance indicates how  
374 much each input variable contributes to the model's predictive accuracy by measuring  
375 the decrease in impurity or error when the feature is used to split data (Gregorutti et  
376 al., 2017). In the VIS+IR model, the top-ranked predictors are CTH and cloud top  
377 temperature (CTT) from the H8/AHI Level-2 product (see Fig. B1 in Appendix B). It  
378 is important to note that  $D_{COT}$  is a crucial and sensitive factor for these ML-based  
379 algorithms. Retrieving CBH samples with relatively low  $D_{COT}$  remains challenging  
380 due to the low signal-to-noise ratio when  $D_{COT}$  is low (Lin et al., 2022). To address  
381 this issue, samples with  $D_{COT}$  less than 1.6 are filtered in the VIS+IR model, and  
382 samples with relatively large BTs at Channel-14 are filtered in the IR-single model.  
383 This filtering process significantly improves the R value from 0.869 to 0.922 in the  
384 VIS+IR model and from 0.868 to 0.911 in the IR-single model. For more details on  
385 the algorithm optimization, please refer to Appendix B.

386 In this study, the H8/AHI satellite CBH data retrieved by the four algorithms  
387 mentioned before are matched spatiotemporally with the 2B-CLDCLASS-LIDAR  
388 cloud product from joint CloudSat/CALIPSO observations in 2017. In this process,  
389 the nearest distance matching method is employed, ensuring that collocating the  
390 closest points and the observation time difference between the CloudSat/CALIPSO  
391 observation point and the matched Himwari-8 data is less than 5 minutes (Noh et al.,  
392 2017). As in earlier study (Min et al., 2020), we also used 70% of the matched data  
393 for training and 30% of an independent sample for validation. Figure 1 displays a  
394 comparison of CBH results over the full disk at 02:00 UTC on January 1, 2017,  
395 retrieved by the GEO IDPS algorithm, the GEO CLAVR-x algorithm, the RF VIS+IR

396 algorithm, and the RF IR-single algorithm for all cloud conditions including single  
397 and multilayer cloud scenes. A similar distribution pattern and magnitude of CBHs  
398 retrieved by these four independent algorithms can be observed in Figure 1. However,  
399 notable differences exist between physics-based and ML-based algorithms. Further  
400 comparisons are conducted and analyzed with spaceborne and ground-based lidar and  
401 radar observations in the subsequent sections of this study.

402

## 403 4 Results and Discussions

### 404 4.1 Comparisons with the joint CloudSat/CALIPSO cloud base height product

#### 405 4.1.1 Joint scatter plots

406 Figure 2 presents the density scatter plot of the CBHs retrieved from the GEO  
407 IDPS and GEO CLAVR-x algorithms compared with the CBHs from the joint  
408 CloudSat/CALIPSO product, along with the related scores of MAE, MBE, RMSE,  
409 and R calculated and labeled in each panel. The calculated R exceeds the 95%  
410 significance level ( $p < 0.05$ ). For the GEO IDPS algorithm, the R is 0.62, the MAE is  
411 1.83 km, and the MBE and RMSE are -0.23, and 2.64 km (Fig. 2a). In comparison,  
412 Seaman et al., (2017) compared the operational VIIRS CBH product retrieved by the  
413 similar SNPP/VIIRS IDPS algorithm with the CloudSat CBH results. In their results,  
414 the R is 0.57, and the RMSE is 2.3 km. For the new GEO CLAVR-x algorithm (Fig.  
415 2b), the R is 0.645, and the RMSE is 2.91 km. The larger RMSE from two  
416 independent physics-based CBH algorithms demonstrate a slightly poorer  
417 performance and precision of these retrieval algorithms for GEO satellites.  
418 Particularly, the larger RMSEs (2.64, and 2.91 km) indicate weaker stabilities of the  
419 GEO IDPS and CLAVR-x CBH algorithms, compared with VIIRS CBH product  
420 (Seaman et al., 2017). In this figure, more samples can be found near the 1:1 line,  
421 implying the good quality of retrieved CBHs. However, in stark contrast, quite a  
422 number of CBH samples retrieved by both GEO IDPS and GEO CLAVR-x  
423 algorithms (compared with the official VIIRS CBH product) fall below 1.0 km,  
424 indicating relatively large errors when compared with the joint CloudSat/CALIPSO  
425 CBH product. Moreover, Figure 2 reveals that relatively large errors are also found in  
426 the CBHs lower than 2 km for the four independent algorithms, primarily caused by  
427 the weak penetration ability of VIS or IR bands on thick and low clouds.

删除了:26

删除了:2

删除了:2

删除了:(

删除了:,

删除了:69

删除了:7

删除了:2

436 Referring to the joint CloudSat/CALIPSO CBH product, Figures 2c and 2d  
 437 present the validations of the CBH results retrieved from two ML-based algorithms  
 438 using the VIS+IR (only retrieving the CBH during the daytime) and IR-single models.  
 439 Figure 2c demonstrates better consistency of CBH between the VIS+IR model and the  
 440 joint CloudSat/CALIPSO product with  $R = 0.91$ ,  $MAE = 0.82$  km,  $MBE = 0.43$  km,  
 441 and  $RMSE = 1.71$  km. Figure 2d also displays a relatively high  $R$  of 0.876 when  
 442 validating the IR-single model, with  $MAE = 0.88$ ,  $MBE = -0.45$ , and  $RMSE = 2.00$ .  
 443 Therefore, both VIS+IR and IR-single models can obtain high-quality CBH retrieval  
 444 results from geostationary imager measurements. In comparison, previous studies also  
 445 proposed similar ML-based algorithms for estimating CBH using FY-4A satellite  
 446 imager data. For example, Tan et al. (2020) used the variables of CTH,  $D_{COT}$ ,  $R_{eff}$ ,  
 447 cloud water path, longitude/latitude from FY-4A imager data to build the training and  
 448 prediction model and obtained CBH with  $MAE=1.29$  km and  $R=0.80$ . In this study,  
 449 except CTH, the other Level-2 products and geolocation data (longitude/latitude) used  
 450 in (Tan et al., 2020) are abandoned, while the matched atmospheric profile products  
 451 (such as temperature and relative humidity) from NWP data are added. These changes  
 452 in ML-based model training and prediction lead to more accurate CBH retrieval  
 453 results. Note that, in accordance with the previous study conducted by Noh et al.  
 454 (2017), we excluded CBH samples obtained from CloudSat/CALIPSO that were  
 455 smaller than 1 km in our comparisons. This exclusion was primarily due to the  
 456 presence of ground clutter contamination in the CloudSat CPR data (Noh et al., 2017).

#### 457 4.1.2 Test case

458 Figure 3 displays two cross-sections of CBH from various sources overlaid with  
 459 CloudSat radar reflectivity (unit: dBZ) for spatiotemporally matched cases. The  
 460 periods covered are from 03:16 to 04:55 UTC on January 13, 2017 (154.0°E–160.0°E;  
 461 40.56°S–53.39°S) and from 05:38 to 07:17 UTC on January 14, 2017 (107.1°E–  
 462 107.8°E; 8.35°N–11.57°N). The CloudSat radar reflectivity and joint  
 463 CloudSat/CALIPSO product provide insights into the vertical structure or distribution  
 464 of clouds and their corresponding CBHs. The results from the four GEO CBH  
 465 retrieval algorithms (GEO IDPS, GEO CLAVR-x, RF VIS+IR model, and RF  
 466 IR-single model) mentioned earlier are individually marked with different markers in  
 467 each panel. According to Figure 3a, the GEO IDPS algorithm faces challenges in  
 468 accurately retrieving CBHs for geometrically thicker cloud samples near 157°E.  
 469 Optically thick mid- and upper-level cloud layers may obscure lower-level cloud

删除了: 05

删除了: 17

删除了: 25

删除了: 06

删除了: 2

删除了: 4

删除了: 1.995

删除了: (

删除了: ,

删除了: (

删除了: ,

481 layers. However, the CBH results retrieved by the GEO IDPS algorithm near 155°E  
482 (in Fig. 3a) and 107.4°E (in Fig. 3b) align with the joint CloudSat/CALIPSO CBH  
483 product. It is worth noting that the inconsistency observed between 107.2°E and  
484 107.3°E in Figure 3b, specifically regarding the CBHs around 1 km obtained from  
485 CloudSat/CALIPSO, can likely be attributed to ground clutter contamination in the  
486 CloudSat CPR data (Noh et al., 2017). The GEO CLAVR-x algorithm achieves  
487 improved CBH results compared to the GEO IDPS algorithm. It can even retrieve  
488 CBHs for some thick cloud samples that are invalid when using the GEO IDPS  
489 algorithm. However, the CBHs from the GEO CLAVR-x algorithm are noticeably  
490 higher than those from the joint CloudSat/CALIPSO product. In contrast, the CBHs  
491 from the two ML-based algorithms show substantially better results than those from  
492 the other two physics-based algorithms. Particularly, the ML-based VIS+IR model  
493 algorithm yields the best CBH results. However, compared with those from the two  
494 physics-based algorithms, the CBHs from the two ML-based algorithms still exhibit a  
495 significant error around 5 km.

#### 496 **4.2 Comparisons with the ground-based lidar and cloud radar measurements**

497 Lidar actively emits laser [pulses](#) in different spectral bands into the air. When the  
498 laser signal encounters cloud particles during transmission, a highly noticeable  
499 backscattered signal is generated and received (Omar et al., 2009). The lidar return  
500 [signal of cloud droplets](#) is markedly distinct from atmospheric aerosol scattering  
501 signals and noise, making CBH easily obtainable from the signal difference or  
502 mutation (Sharma et al., 2016). In this study, continuous ground-based lidar data from  
503 the Twin Astronomy Manor in Lijiang City, Yunnan Province, China (26.454°N,  
504 100.0233°E, altitude = 3175 m) are used to evaluate the diurnal cycle characteristics  
505 of CBHs retrieved using GEO satellite algorithms (Young and Vaughan, 2009). The  
506 geographical location and photo of this station are shown in Figure 4.

##### 507 **4.2.1 Comparison of CBH retrievals from ground and satellite data**

508 The ground-based lidar data at Lijiang station on December 6, 2018, and January  
509 8, 2019, are selected for validation. In fact, this lidar was primarily used for the  
510 calibration of ground-based lunar radiation instruments. During the two-month  
511 observation period (from December of 2018 to January of 2019), it was always  
512 operated only under clear sky conditions, resulting in the capture of cloud data on just  
513 two days. These two days have been cloudy, with stratiform clouds at an altitude of

514 around 5 km and no precipitation occurring. The number of available and  
515 spatiotemporally matched CBH sample points from ground-based lidar is 78 and 64  
516 on December 6, 2018, and January 8, 2019, respectively. Figure 5a and 5b show the  
517 point-to-point CBH comparisons between ground-based lidar and four GEO satellite  
518 CBH algorithms on December 6, 2018, and January 8, 2019. It is worth noting that  
519 the retrieved CBHs of the two physics-based algorithms on December 6, 2018, are in  
520 good agreement with the reference values from the lidar measurements, and, in  
521 particular, the GEO CLAVR-x algorithm can obtain better results. From the results on  
522 January 8, 2019, more accurate diurnal cycle characteristics of CBHs are revealed by  
523 the GEO CLAVR-x algorithm than by the GEO IDPS algorithm.

524 Compared with the CBHs measured by ground-based lidar, the statistics of the  
525 results retrieved from the GEO IDPS algorithm are  $R = 0.67$ ,  $MAE = 3.09$  km,  $MBE$   
526  $= 0.86$  km, and  $RMSE = 3.61$  km (Fig. 5c). However, for cloud samples with CBH  
527 below 7.5 km, the GEO IDPS algorithm shows an obvious underestimation of CBH in  
528 Figure 5c. For the GEO CLAVR-x algorithm, it can also be seen that the matched  
529 samples mostly lie near the 1:1 line with  $R = 0.77$  (the optimal CBH algorithm),  $MAE$   
530  $= 1.32$  km,  $MBE = 0.22$  km, and  $RMSE = 1.60$  km. In addition, this figure also shows  
531 the CBH comparisons between the ML-based VIS+IR model/IR-single model  
532 algorithms and the lidar measurements, revealing that the retrieved CBH results from  
533 the ML-based VIS+IR model are better than those from the ML-based IR-single  
534 model algorithm. The comparison results between the CBHs of the ML-based VIS+IR  
535 model algorithm and the lidar measurements are around the 1:1 line, with smaller  
536 errors and  $R = 0.60$ . In contrast, the  $R$  between the CBHs of the ML-based IR-single  
537 model algorithm and the lidar measurements is only  $0.50$ , with a relatively large error.  
538 By comparing the retrieved CBHs with the lidar measurements at Lijiang station, it  
539 indicates that CBH results from two physics-based algorithms are remarkably more  
540 accurate, particularly that the GEO CLAVR-x algorithm can well capture diurnal  
541 variation of CBH.

542 To further assess the accuracy and quality of the diurnal cycle of CBHs retrieved  
543 with these algorithms, CBHs from another ground-based cloud radar dataset covering  
544 the entire year of 2017 are also collected and used in this study. The observational  
545 instrument is a Ka-band (35 GHz) Doppler millimeter-wave cloud radar (MMCR)  
546 located at the Beijing Nanjiao Weather Observatory (a typical urban observation site)  
547 (39.81°N, 116.47°E, altitude = 32 m; see Fig. 4), performing continuous and routine

删除了: 3

删除了: 5

删除了: 09

删除了: 3

删除了: 19

删除了: 2

删除了: 598

删除了: 599

删除了: 494



557 observations. The MMCR provides a specific vertical resolution of 30 m and a  
558 temporal resolution of 1 minute for single profile detection, based on the radar  
559 reflectivity factor. In a previous study (Zhou et al., 2019), products retrieved by this  
560 MMCR were utilized to investigate the diurnal variations of CTH and CBH, and  
561 comparisons were made between MMCR-derived CBHs and those derived from a  
562 Vaisala CL51 ceilometer. The former study also found that the average R of CBHs  
563 from different instruments reached up to 0.65. It is worth noting that the basic physics  
564 principle for detecting cloud base height from both spaceborne cloud profiling radar  
565 and ground-based cloud radar and lidar measurements is the same. All these  
566 algorithms of detecting CBH are based on the manifest change of return signals  
567 between CBH and the clear sky atmosphere in the vertical direction (Huo et al., 2019;  
568 Ceccaldi et al., 2013). The diurnal variation of cloud base height over land is  
569 primarily influenced by solar heating, causing the cloud base to rise in the morning  
570 and reach its peak by midday. As the surface cools in the afternoon and evening, the  
571 cloud base lowers, playing a crucial role in weather patterns and forecasting (Zheng et  
572 al., 2020). Due to the density of points in the one-year time series, the point-to-point  
573 CBH comparison results for the entire year are not displayed here (monthly results are  
574 shown in the supplementary document), we only show 4 days results in the following  
575 Figure 6. Therefore, it is essential to rigorously compare the ML-based algorithm with  
576 ground-based observations to determine its ability to adapt to the daily variations in  
577 cloud base height caused by natural factors. The joint spaceborne CloudSat/CALIPSO  
578 detection might face limitations in penetrating extremely dense, optically thick, or  
579 areas with heavy precipitation clouds. Hence, in comparison, the CBH values  
580 gathered from ground-based lidar and cloud radar measurements are expected to be  
581 more accurate than the data derived from spaceborne CloudSat/CALIPSO detection.

582 Similar to Figure 5, Figure 6 presents two sample groups of CBH results from the  
583 cloud radar at Beijing Nanjiao station relative to the matched CBHs from the four  
584 retrieval algorithms (GEO IDPS, GEO CLAVR-x, ML-based IR-single, ML-based  
585 VIS+IR) on April 9–10 and July 26–28, 2017. Similar to the results at Lijiang station  
586 discussed in Figure 5, we observe better and more robust performances in retrieving  
587 diurnal cycle characteristics of CBH from the two physics-based CBH retrieval  
588 algorithms. In contrast, more underestimated CBH samples are retrieved by the two  
589 ML-based algorithms.

#### 590 4.2.2 Diurnal cycle analysis of CBH retrieval accuracy

删除了: As well known,

删除了: t

593 To further investigate the diurnal cycle characteristics of retrieved CBH from  
594 GEO satellite imager measurements, Figure 7 presents box plots of the hourly CBH  
595 errors (relative to the results of cloud radar at Beijing Nanjiao station) in 2017 from  
596 the four different CBH retrieval algorithms. Remarkably, there are significant  
597 underestimations of the CBHs retrieved from the two ML-based algorithms. The  
598 ML-based VIS+IR method achieves relatively better results than the ML-based  
599 IR-single method during the daytime. Comparing the two ML-based algorithms, the  
600 errors of the IR-single model algorithm have a similar standard deviation (2.80 km) to  
601 those of the VIS+IR model algorithm (2.69 km) during the daytime. For the IR-single  
602 model algorithm, it can be applied during both daytime and nighttime, its nighttime  
603 performance degrades slightly, with an averaged RMSE (3.88 km) higher than that of  
604 daytime (3.56 km). The nighttime CBH of the IR-single model algorithm is the only  
605 choice that should be used with discretion.

606 Figure 8 shows the comparisons of hourly MAE, MBE, RMSE, and R relative to  
607 the CBHs from the cloud radar at Beijing Nanjiao station during daytime between  
608 four retrieval algorithms in 2017. The RMSE of the two ML-based algorithms shows  
609 stable diurnal variation. It is noted that all algorithms have lower R at sunrise, around  
610 07:00 local time, which improve as the day progresses. However, the GEO CLAVR-x  
611 algorithm stands out for its relatively higher and more stable in R and RMSE during  
612 daytime.

613 Figure 9a displays scatter plots and relevant statistics of the CBHs retrieved from  
614 the GEO IDPS algorithm against the CBHs from cloud radar. The CBHs from the  
615 GEO IDPS algorithm align well with the matched CBHs from cloud radar at Beijing  
616 Nanjiao station, with  $R = 0.52$ ,  $MAE = 2.08$  km,  $MBE = 1.17$  km, and  $RMSE = 2.67$   
617 km. In Figure 9b, the GEO CLAVR-x algorithm shows better results with  $R = 0.57$ ,  
618  $MAE = 2.06$  km,  $MBE = -0.20$  km, and  $RMSE = 2.60$  km. It is not surprising that  
619 Figs. 8c and 8d reveal obvious underestimated CBH results from the two ML-based  
620 CBH algorithms. Particularly, the CBH results from the ML-based VIS+IR model  
621 algorithm concentrate in the range of 2.5 km to 5 km. Therefore, Figure 5 to Figure 9  
622 further substantiates the weak diurnal variations captured by ML-based techniques,  
623 primarily attributed to the scarcity of comprehensive CBH training samples  
624 throughout the entire day. Besides, although the two robust physics-based algorithms  
625 of GEO IDPS and GEO CLAVR-x (the optimal one) can retrieve high-quality CBHs  
626 from H8/AHI data, especially the diurnal cycle of CBH during the daytime, they still

删除了: 15

删除了: 78

删除了: 68

删除了: 69

删除了: 3

删除了: 59

删除了: 4

删除了: 1

635 struggle to retrieve CBHs below 1 km.

## 636 5. Conclusions and discussion

637 To explore and argue the optimal and most robust CBH retrieval algorithm from  
638 geostationary satellite imager measurements, particularly focusing on capturing the  
639 typical diurnal cycle characteristics of CBH over land, this study employs four  
640 different retrieval algorithms (two physics-based and two ML-based algorithms).  
641 High spatiotemporal resolution CBHs are retrieved using the H8/AHI data from 2017  
642 and 2019. To assess the accuracies of the retrieved CBHs, point-to-point validations  
643 are conducted using spatiotemporally matched CBHs from the joint  
644 CloudSat/CALIOP product, ground-based lidar and cloud radar observations in China.  
645 The main findings and conclusions are outlined below.

删除了: as well as

646 Four independent CBH retrieval algorithms, namely physics-based GEO IDPS,  
647 GEO CLAVR-x, ML-based VIS+IR, and ML-based IR-single, have been developed  
648 and utilized to retrieve CBHs from GEO H8/AHI data under the assumption of single  
649 layer cloud. The two physics-based algorithms utilize cloud top and optical property  
650 products from AHI as input parameters to retrieve high spatiotemporal resolution  
651 CBHs, with operations limited to daytime. In contrast, the ML-based VIS+IR model  
652 and IR-single model algorithms use the matched joint CloudSat/CALIOP CBH  
653 product as true values for building RF prediction models. Notably, the ML-based  
654 IR-single algorithm, which relies solely on infrared band measurements, can retrieve  
655 CBH during both day and night.

656 The accuracy of CBHs retrieved from the four independent algorithms is verified  
657 using the joint CloudSat/CALIOP CBH products for the year 2017. The GEO IDPS  
658 algorithm shows an R of 0.62 and an RMSE of 2.64 km. The GEO CLAVR-x  
659 algorithm provides more accurate CBHs with an R of 0.65 and RMSE of 2.91 km.  
660 After filtering samples with optical thickness less than 1.6 and brightness temperature  
661 (at 11  $\mu\text{m}$  band) greater than 281 K, the ML-based VIS+IR and ML-based IR-single  
662 algorithms achieve higher accuracy with an R(RMSE) of 0.92(1.21 km) and 0.91(1.42  
663 km), respectively. This indicates strong agreement between the two ML-based CBH  
664 algorithms and the CloudSat/CALIOP CBH product.

删除了: 2

删除了: 47

删除了: 2

删除了: 4

删除了: 1

删除了: 15

665 However, in stark contrast, the results from the physics-based algorithms (with R  
666 and RMSE of 0.59/2.86 km) are superior to those from the ML-based algorithms

删除了: 2

675 (with R and RMSE of 0.39/3.88 km) when compared with ground-based CBH  
676 observations such as lidar and cloud radar. In the comparison with the cloud radar at  
677 Beijing Nanjiao station in 2017, the R of the GEO CLAVR-x algorithm is 0.57, while  
678 the R of the GEO IDPS algorithm is 0.52. Meanwhile, notable differences are  
679 observed in the CBHs between both ML-based algorithms. Similar conclusions are  
680 also evident in the 2-day comparisons at Yunnan Lijiang station.

删除了: 85

删除了: 3

删除了: 15

681 The CBH results from the two ML-based algorithms ( $R > 0.91$ ) can likely be  
682 attributed to the use of the same training and validation dataset source as the joint  
683 CloudSat/CALIOP product. However, this dataset has limited spatial coverage and  
684 small temporal variation, potentially limiting the representativeness of the training  
685 data. In contrast, the GEO CLAVR-x algorithm demonstrates the best performance  
686 and highest accuracy in retrieving CBH from geostationary satellite data. Notably, its  
687 results align well with those from ground-based lidar and cloud radar during the  
688 daytime. However, both physics-based methods, utilizing CloudSat CPR data for  
689 regression, struggle to accurately retrieve CBHs below 1 km, as the lowest 1 km  
690 above ground level of this data is affected by ground clutter.

691 Additionally, despite utilizing the same physics principles in spaceborne and  
692 ground-based lidar/radar CBH algorithms, the previous study (Thorsen et al., 2011)  
693 has highlighted differences in profiles between them. Therefore, this factor induced  
694 by detection principle could contribute to the relatively poorer results in CBH  
695 retrieval by ML-based algorithms compared to ground-based lidar and radar. The  
696 analysis and discussion above suggest that ML-based algorithms are constrained by  
697 the size and representativeness of their datasets.

698 Ideally, we guess that including more spaceborne cloud profiling radars with  
699 varying passing times (covering the entire day) in the training dataset could improve  
700 the machine learning technique, potentially leading to a higher-quality CBH product  
701 with more comprehensive observations. The CBH product using ML-based  
702 algorithms should continue to be improved in future work. Particularly, exploring the  
703 joint ML-physics-based method presents a promising direction, which can address the  
704 complexities and challenges in retrieving cloud properties. By integrating established  
705 physical relationships into ML models, we can potentially enhance the accuracy and  
706 reliability of predictions. This approach not only leverages the strengths of both  
707 physics-based models and data-driven techniques but also offers a pathway to more  
708 robust and interpretable solutions in atmospheric sciences. At present, we will focus

712 on developing physics-based algorithms for cloud base height for the next generation  
713 of geostationary meteorological satellites, to support the application of these products  
714 in weather and climate domains.

715 Besides, at night, current GEO satellite imaging instruments encounter  
716 challenges in accurately determining CBH due to limited or absent solar illumination.  
717 Because it is unable to retrieve cloud optical depth in the visible band, the current  
718 method faces limitations. However, there is potential for enhanced accuracy in  
719 deriving cloud optical and microphysical properties, as well as CBH, by incorporating  
720 the Day/Night Band (DNB) observations during nighttime in the future (Walther et al.,  
721 2013).

722

723

724 *Data availability.* The authors would like to acknowledge NASA, JMA, Colorado  
725 State University, and NOAA for freely providing the MODIS  
726 (<https://ladsweb.modaps.eosdis.nasa.gov/search>), CloudSat/CALIOP  
727 (<https://www.cloudsat.cira.colostate.edu/>), Himawari-8 (<ftp.ptree.jaxa.jp>), and GFS  
728 NWP (<ftp://nomads.ncdc.noaa.gov/GFS/Grid4>) data online, respectively.

729

730

731 *Author contributions.* MM proposed the essential research idea. MW, MM, JL, HL,  
732 BC, and YL performed the analysis and drafted the manuscript. ZY and NX provided  
733 useful comments. All the authors contributed to the interpretation and discussion of  
734 results and the revision of the manuscript.

735

736

737 *Competing interests.* The authors declare that they have no conflict of interest.

738

739

740 *Acknowledgements.* The authors would like to acknowledge NASA, JMA, University  
741 of Colorado, and NOAA for freely providing satellite data online, respectively. The  
742 authors thank NOAA, NASA, and their VIIRS algorithm working groups (AWG) for  
743 freely providing the VIIRS cloud base height algorithm theoretical basic

744 documentations (ATBD). In addition, the authors appreciate the power computer tools  
745 developed by the Python and scikit-learn groups (<http://scikit-learn.org>). Besides the  
746 authors also thank Rundong Zhou and Pan Xia for drawing some pictures of this  
747 manuscript. Last but not the least, the authors sincerely thank Prof. Yong Zhang and  
748 Prof. Jianping Guo for freely providing cloud base height results retrieved by  
749 ground-based cloud radar at Beijing Nanjiao station. This work was supported partly  
750 by the Guangdong Major Project of Basic and Applied Basic Research (Grant  
751 2020B0301030004), National Natural Science Foundation of China under Grants  
752 42175086 and U2142201, FengYun Meteorological Satellite Innovation Foundation  
753 under Grant FY-APP-ZX-2022.0207, the Innovation Group Project of Southern  
754 Marine Science and Engineering Guangdong Laboratory (Zhuhai) (No.  
755 SML2023SP208), and the Science and Technology Planning Project of Guangdong  
756 Province (2023B1212060019). We would like to thank the editor and anonymous  
757 reviewers for their thoughtful suggestions and comments.

758

759

## 760 **Appendix A**

761 Based on the previously discussed description of two physics-based cloud base  
762 height (CBH) retrieval algorithms (GEO IDPS and GEO CLAVR-x retrieval  
763 algorithms), cloud products such as cloud top height (CTH), effective particle radius  
764 ( $R_{\text{eff}}$ ), and cloud optical thickness ( $D_{\text{COT}}$ ) will be utilized in both algorithms. To  
765 validate the reliability of these cloud products derived from the Advanced Himawari  
766 Imager (AHI) aboard the Himawari-8 (H8), a pixel-by-pixel comparison is conducted  
767 with analogous MODIS Collection-6.1 Level-2 cloud products. Both Aqua and Terra  
768 MODIS Level-2 cloud products (MOD06 and MYD06) are accessible for free  
769 download from the MODIS official website. For verification purposes, the  
770 corresponding Level-2 cloud products from January, April, July, and October of 2018  
771 are chosen to assess CTH,  $D_{\text{COT}}$ , and  $R_{\text{eff}}$  retrieved by H8/AHI.

772 Figure S2 (in the supplementary document) shows the spatiotemporally matched  
773 case comparisons of CTH,  $D_{\text{COT}}$  and  $R_{\text{eff}}$  from H8/AHI and Terra/MODIS (MYD06)  
774 at 03:30 UTC on January 15, 2018. It can be seen that the CTH,  $D_{\text{COT}}$  and  $R_{\text{eff}}$  from

775 H8/AHI are in good agreement with the matched MODIS cloud products. However,  
776 there are still some differences in  $R_{\text{eff}}$  at the regions near 35°N, 110°E in Figures S2d  
777 and S2c. The underestimated  $R_{\text{eff}}$  values from H8/AHI relative to MODIS have been  
778 reported in previous studies. Letu et al., (2019) compared the ice cloud products  
779 retrieved from AHI and MODIS, and concluded that the  $R_{\text{eff}}$  from both products differ  
780 remarkably in the ice cloud region and the  $D_{\text{COT}}$  from them are roughly similar.  
781 However, the  $D_{\text{COT}}$  from AHI data is higher in some areas. Looking again at the cloud  
782 optical thickness that at the same time, the slight underestimation of H8/AHI  $D_{\text{COT}}$   
783 can be found in Figures S2e and S2f. Figure S3 (in the supplementary document)  
784 shows another case at 02:10 UTC on January 15, 2018. Despite of the good  
785 consistence between H8/AHI and MODIS cloud products, there are slight differences  
786 in CTH in the area around 40°S–40.5°S, 100°E–110°E in Figs. S3a and S3b. Besides,  
787 as shown in Figure S2, there are still underestimations in the  $R_{\text{eff}}$  of H8/AHI.

788 To further compare and validate these three H8/AHI cloud products, the  
789 spatiotemporally matched samples from H8/AHI and Aqua/Terra MODIS in four  
790 months of 2018 are counted within the three intervals of 0.1 km (CTH), 1.0  $\mu\text{m}$  ( $R_{\text{eff}}$ ),  
791 and 1 ( $D_{\text{COT}}$ ) in Figure S4 (in the supplementary document). The corresponding mean  
792 absolute error, mean bias error, RMSE and  $R$  values are also calculated and marked in  
793 each subfigure. As can be seen, the  $R$  of CTH is around 0.75 in all four months and is  
794 close to 0.8 in August. The results of  $D_{\text{COT}}$  show the highest  $R$ , reaching above 0.8. In  
795 contrast, the underestimation trend in  $R_{\text{eff}}$  is also shown in this figure. These different  
796 consistencies between two satellite-retrieved cloud products may be attributed to: (1)  
797 different spatiotemporal resolutions between H8/AHI and MODIS; (2) different  
798 wavelength bands, bulk scattering model, and specific algorithm used for retrieving  
799 cloud products; (3) different view zenith angle between GEO and low-earth-orbit  
800 satellite platforms (Letu et al., 2019). In addition, other external factors such as  
801 surface type also can affect the retrieval of cloud product. However, according to  
802 Figure S4, the bulk of the analyzed samples are still around the 1:1 line, indicating the  
803 good quality of H8/AHI cloud products.

804

## 805 Appendix B

806 The ML-based visible (VIS)+infrared (IR) model algorithm mentioned above  
807 uses 230 typical variables (see Table 1) as model predictors, and the importance  
808 scores of top-30 predictors are ranked in Figure S5 (in the supplementary document).

删除了:(

删除了:,

811 It can be seen that the most important variables are CTH and CTT, and  $D_{\text{COT}}$  is an  
812 important or sensitive factor affecting these two quantities. A sensitivity test is also  
813 performed to further investigate the potential influence of  $D_{\text{COT}}$  on the CBH retrieval  
814 by the VIS+IR model (see Table S1 in the supplementary document). From Figure  
815 S7a, we find that the samples with  $D_{\text{COT}}$  lower than 5 cause the relatively large CBH  
816 errors compared with the matched CBHs from the joint CALIPSO (Cloud-Aerosol  
817 Lidar and Infrared Pathfinder Satellite Observation)/CloudSat product.

818 According to the results in this Figure S7b, we may filter the samples with  
819 relatively small  $D_{\text{COT}}$  to further improve the accuracy of CBH retrieval by the VIS+IR  
820 model (see Table S1). Figure S7b shows that after filtering the samples with the  $D_{\text{COT}}$   
821 less than 1.6, the  $R$  increases from 0.895 to 0.922, implying a better performance of  
822 CBH retrieval. According to the ranking of predictor importance (see Fig. S6 in the  
823 supplementary document), we also conduct another sensitivity test on the BT  
824 observed by H8/AHI IR Channel-14 (Cha14) at 11  $\mu\text{m}$ , which plays an important role  
825 in the IR-single model. Figure S7c shows that the BT values of H8/AHI Channel-14  
826 ranges from 160 K to 316 K, and the samples with BT higher than 300 K show large  
827 CBH errors. Similarly, by filtering the samples with BT higher than 281 K, we can get  
828 a better IR-single model algorithm for retrieving high-quality CBH (see Table S2 in  
829 the supplementary document). Figure S7d also proves that the  $R$  value increases from  
830 0.868 to 0.911.

831  
832  
833  
834  
835  
836  
837  
838  
839  
840  
841



842 **Reference**

- 843 Aydin, K. and Singh, J.: Cloud Ice Crystal Classification Using a 95-GHz Polarimetric Radar, *Journal of*  
844 *Atmospheric and Oceanic Technology*, 21, 1679–1688, <https://doi.org/10.1175/JTECH1671.1>, 2004.
- 845 Baker, N.: Joint Polar Satellite System (JPSS) VIIRS Cloud Base Height Algorithm Theoretical Basis  
846 Document (ATBD), 2011.
- 847 Baum, B., Menzel, W. P., Frey, R., Tobin, D., Holz, R., and Ackerman, S.: MODIS cloud top property  
848 refinements for Collection 6, *Journal of Applied Meteorology and Climatology*, 51, 1145-1163,  
849 10.1175/JAMC-D-11-0203.1, 2012.
- 850 Bessho, K., Date, K., Hayashi, M., Ikeda, A., Imai, T., Inoue, H., Kumagai, Y., Miyakawa, T., Murata, H.,  
851 Ohno, T., Okuyama, A., Oyama, R., Sasaki, Y., Shimazu, Y., Shimoji, K., Sumida, Y., Suzuki, M., Taniguchi,  
852 H., Tsuchiyama, H., Uesawa, D., Yokota, H., and Yoshida, R.: An introduction to Himawari-8/9—Japan's  
853 new-generation geostationary meteorological satellites, *Journal of the Meteorological Society of*  
854 *Japan*, 94, 151-183, 10.2151/jmsj.2016-009, 2016.
- 855 Breiman, L.: Random forests, *Machine Learning*, 45, 5-32, 2001.
- 856 Ceccaldi, M., Delanoë, J., Hogan, R. J., Pounder, N. L., Protat, A., and Pelon, J.: From CloudSat-CALIPSO  
857 to EarthCare: Evolution of the DARDAR cloud classification and its comparison to airborne radar-lidar  
858 observations, *Journal of Geophysical Research: Atmospheres*, 118, 7962-7981, 10.1002/jgrd.50579,  
859 2013.
- 860 Forsythe, J. M., Haar, T. H. V., and Reinke, D. L.: Cloud-Base height estimates using a combination of  
861 *Meteorological Satellite Imagery and Surface Reports*, *Journal of Applied Meteorology and Climatology*,  
862 39, 2336–2347, [https://doi.org/10.1175/1520-0450\(2000\)039<2336:CBHEUA>2.0.CO;2](https://doi.org/10.1175/1520-0450(2000)039<2336:CBHEUA>2.0.CO;2), 2000.
- 863 Gregorutti, B., Michel, B., and Saint-Pierre, P.: Correlation and variable importance in random forests,  
864 *Statistics and Computing*, 27, 659-678, 10.1007/s11222-016-9646-1, 2017.
- 865 Håkansson, N., Adok, C., Thoss, A., Scheirer, R., and Hörnquist, S.: Neural network cloud top pressure  
866 and height for MODIS, *Atmospheric Measurement Techniques*, 11, 3177–3196,  
867 10.5194/amt-11-3177-2018, 2018.
- 868 Hansen, B.: A Fuzzy Logic–Based Analog Forecasting System for Ceiling and Visibility, *Weather and*  
869 *Forecasting*, 22, 1319-1330, 10.1175/2007waf2006017.1, 2007.
- 870 Hartmann, D. L. and Larson, K.: An important constraint on tropical cloud - climate feedback, *Geophys*  
871 *Res Lett*, 29, 12-11-12-14, 10.1029/2002gl015835, 2002.
- 872 Heidinger, A. and Pavolonis, M.: Gazing at cirrus clouds for 25 years through a split window, part 1:  
873 *Methodology*, *Journal of Applied Meteorology and Climatology*, 48, 1110-1116,  
874 10.1175/2008JAMC1882.1, 2009.
- 875 Heidinger, A. K., Bearson, N., Foster, M. J., Li, Y., Wanzong, S., Ackerman, S., Holz, R. E., Platnick, S., and  
876 Meyer, K.: Using sounder data to improve cirrus cloud height estimation from satellite imagers,  
877 *Journal of Atmospheric and Oceanic Technology*, 36, 1331-1342, 10.1175/jtech-d-18-0079.1, 2019.
- 878 Heymsfield, A. J., Bansemir, A., Matrosov, S., and Tian, L.: The 94-GHz radar dim band: Relevance to  
879 ice cloud properties and CloudSat, *Geophys. Res. Lett.*, 35, 10.1029/2007GL031361, 2008.
- 880 Hirsch, E., Agassi, E., and Koren, I.: A novel technique for extracting clouds base height using ground  
881 based imaging, *Atmospheric Measurement Techniques*, 4, 117-130, 10.5194/amt-4-117-2011, 2011.
- 882 Hunt, W. H., Winker, D. M., Vaughan, M. A., Powell, K. A., Lucker, P. L., and Weimer, C.: CALIPSO lidar  
883 description and performance assessment, *J. Atmos. Oceanic. Technol.*, 26, 2009.
- 884 Huo, J., Bi, Y., Lü, D., and Duan, S.: Cloud Classification and Distribution of Cloud Types in Beijing Using  
885 Ka-Band Radar Data, *Advances in Atmospheric Sciences*, 36, 793-803, 10.1007/s00376-019-8272-1,

886 2019.

887 Hutchison, K., Wong, E., and Ou, S. C.: Cloud base heights retrieved during night-time conditions with  
888 MODIS data, *Int J Remote Sens*, 27, 2847-2862, 10.1080/01431160500296800, 2006.

889 Hutchison, K. D.: The retrieval of cloud base heights from MODIS and three-dimensional cloud fields  
890 from NASA's EOS Aqua mission, *Int J Remote Sens*, 23, 5249-5265, 10.1080/01431160110117391,  
891 2002.

892 Iwabuchi, H., Putri, N. S., Saito, M., Tokoro, Y., Sekiguchi, M., Yang, P., and Baum, B. A.: Cloud Property  
893 Retrieval from Multiband Infrared Measurements by Himawari-8, *Journal of the Meteorological*  
894 *Society of Japan. Ser. II*, 96B, 27-42, 10.2151/jmsj.2018-001, 2018.

895 Kalnay, E., Kanamitsu, M., Kistler, R., Collins, W., Deaven, D., Gandin, L., Iredell, M., Saha, S., White, G.,  
896 Woollen, J., Zhu, Y., Leetmaa, A., Reynolds, R., Chelliah, M., Ebisuzaki, W., W.Higgins, Janowiak, J., Mo,  
897 K. C., Ropelewski, C., and Wang, J.: The NCEP NCAR 40-Year Reanalysis Project, 1996.

898 Kühnlein, M., Appelhans, T., Thies, B., and Nauß, T.: Precipitation Estimates from MSG SEVIRI Daytime,  
899 Nighttime, and Twilight Data with Random Forests, *Journal of Applied Meteorology and Climatology*,  
900 53, 2457-2480, 10.1175/jamc-d-14-0082.1, 2014.

901 Letu, H., Nagao, T. M., Nakajima, T. Y., Riedi, J., Ishimoto, H., Baran, A. J., Shang, H., Sekiguchi, M., and  
902 Kikuchi, M.: Ice cloud properties from Himawari-8/AHI next-generation geostationary satellite:  
903 Capability of the AHI to monitor the DC cloud generation process, *IEEE Transactions on Geoscience*  
904 *and Remote Sensing*, 57, 3229-3239, 10.1109/tgrs.2018.2882803, 2019.

905 Li, Y., Yi, B., and Min, M.: Diurnal variations of cloud optical properties during day-time over China  
906 based on Himawari-8 satellite retrievals, *Atmospheric Environment*, 277, 119065,  
907 10.1016/j.atmosenv.2022.119065, 2022.

908 Liang, Y., Min, M., Yu, Y., Wang, X., and Xia, P.: Assessing diurnal cycle of cloud covers of Fengyun-4A  
909 geostationary satellite based on the manual observation data in China, *IEEE Transactions on*  
910 *Geoscience and Remote Sensing*, 61, 10.1109/TGRS.2023.3256365, 2023.

911 Lin, H., Li, Z., Li, J., Zhang, F., Min, M., and Menzel, W. P.: Estimate of daytime single-layer cloud base  
912 height from Advanced Baseline Imager measurements, *Remote Sensing of Environment*, 274, 112970,  
913 10.1016/j.rse.2022.112970, 2022.

914 Lu, X., Mao, F., Rosenfeld, D., Zhu, Y., Pan, Z., and Gong, W.: Satellite retrieval of cloud base height and  
915 geometric thickness of low-level cloud based on CALIPSO, *Atmospheric Chemistry and Physics*, 21,  
916 10.5194/acp-21-11979-2021, 2021.

917 Meerkötter, R. and Bugliaro, L.: Diurnal evolution of cloud base heights in convective cloud fields from  
918 MSG/SEVIRI data *Atmospheric Chemistry and Physics*, 9, 1767–1778, 10.5194/acp-9-1767-2009,  
919 2009.

920 Miller, R. M., Rauber, R. M., Girolamo, L. D., Rilloraza, M., Fu, D., McFarquhar, G. M., Nesbitt, S. W.,  
921 Ziemba, L. D., Woods, S., and Thornhill, K. L.: Influence of natural and anthropogenic aerosols on cloud  
922 base droplet size distributions in clouds over the South China Sea and West Pacific, *Atmospheric*  
923 *Chemistry and Physics*, 23, 8959–8977, 10.5194/acp-23-8959-2023, 2023.

924 Miller, S. D., Rogers, M. A., Haynes, J. M., Sengupta, M., and Heidinger, A. K.: Short-term solar  
925 irradiance forecasting via satellite/model coupling, *Solar Energy*, 168, 102-117,  
926 10.1016/j.solener.2017.11.049, 2018.

927 Min, M. and Zhang, Z.: On the influence of cloud fraction diurnal cycle and sub-grid cloud optical  
928 thickness variability on all-sky direct aerosol radiative forcing, *Journal of Quantitative Spectroscopy*  
929 *and Radiative Transfer*, 142, 25-36, 10.1016/j.jqsrt.2014.03.014., 2014.

930 Min, M., Li, J., Wang, F., Liu, Z., and Menzel, W. P.: Retrieval of cloud top properties from advanced  
931 geostationary satellite imager measurements based on machine learning algorithms, *Remote Sensing*  
932 *of Environment*, 239, 111616, 10.1016/j.rse.2019.111616 2020.

933 Min, M., Chen, B., Xu, N., He, X., Wei, X., and Wang, M.: Nonnegligible diurnal and long-term variation  
934 characteristics of the calibration biases in Fengyun-4A/AGRI infrared channels based on the oceanic  
935 drifter data, *IEEE Transactions on Geoscience and Remote Sensing*, 60, 1-15,  
936 10.1109/TGRS.2022.3160450, 2022.

937 Min, M., Wu, C., Li, C., Liu, H., Xu, N., Wu, X., Chen, L., Wang, F., Sun, F., Qin, D., Wang, X., Li, B., Zheng,  
938 Z., Cao, G., and Dong, L.: Developing the science product algorithm testbed for Chinese  
939 next-generation geostationary meteorological satellites: FengYun-4 series, *Journal of Meteorological*  
940 *Research*, 31, 708-719, 10.1007/s13351-017-6161-z, 2017.

941 Noh, Y.-J., Miller, S. D., Seaman, C. J., Haynes, J. M., Li, Y., Heidinger, A. K., and Kulie, M. S.: Enterprise  
942 AWG Cloud Base Algorithm (ACBA), 2022.

943 Noh, Y.-J., Forsythe, J. M., Miller, S. D., Seaman, C. J., Li, Y., Heidinger, A. K., Lindsey, D. T., Rogers, M. A.,  
944 and Partain, P. T.: Cloud-base height estimation from VIIRS. Part II: A statistical algorithm based on  
945 A-Train satellite data, *Journal of Atmospheric and Oceanic Technology*, 34, 585–598,  
946 10.1175/JTECH-D-16-0110.1, 2017.

947 Omar, A., Winker, D., Kittaka, C., Vaughan, M., Liu, Z., Hu, Y., Trepte, C., Rogers, R., Ferrare, R., Kuehn,  
948 R., and Hostetler, C.: The CALIPSO automated aerosol classification and lidar ratio selection algorithm,  
949 *J. Atmos. Oceanic. Technol.*, 26, 1994-2014, 10.1175/2009JTECHA1231, 2009.

950 Platnick, S., Meyer, K. G., King, M. D., Wind, G., Amarasinghe, N., Marchant, B., Arnold, G. T., Zhang, Z.,  
951 Hubanks, P. A., Holz, R. E., Yang, P., Ridgway, W. L., and Riedi, J.: The MODIS cloud optical and  
952 microphysical products: Collection 6 updates and examples from Terra and Aqua, *IEEE Trans Geosci*  
953 *Remote Sens*, 55, 502-525, 10.1109/TGRS.2016.2610522, 2017.

954 Rosenfeld, D., Zheng, Y., Hashimshoni, E., Pohlker, M. L., Jefferson, A., Pohlker, C., Yu, X., Zhu, Y., Liu, G.,  
955 Yue, Z., Fischman, B., Li, Z., Giguzin, D., Goren, T., Artaxo, P., Barbosa, H. M., Poschl, U., and Andreae,  
956 M. O.: Satellite retrieval of cloud condensation nuclei concentrations by using clouds as CCN chambers,  
957 *Proc. Natl. Acad. Sci.*, 113, 5828-5834, 10.1073/pnas.1514044113, 2016.

958 Sassen, K. and Wang, Z.: Classifying clouds around the globe with the CloudSat radar: 1-year of results,  
959 *Geophys. Res. Lett.*, 35, 1-5, doi:10.1029/2007GL032591, 2008.

960 Seaman, C. J., Noh, Y.-J., Miller, S. D., Heidinger, A. K., and Lindsey, D. T.: Cloud-base height estimation  
961 from VIIRS. Part I: Operational algorithm validation against CloudSat, *Journal of Atmospheric and*  
962 *Oceanic Technology*, 34, 567-583, 10.1175/jtech-d-16-0109.1, 2017.

963 Sharma, S., Vaishnav, R., Shukla, M. V., Kumar, P., Kumar, P., Thapliyal, P. K., Lal, S., and Acharya, Y. B.:  
964 Evaluation of cloud base height measurements from Ceilometer CL31 and MODIS satellite over  
965 Ahmedabad, India, *Atmospheric Measurement Techniques*, 9, 711-719, 10.5194/amt-9-711-2016,  
966 2016.

967 Stephens, G. L., Vane, D. G., Boain, R. J., Mace, G. G., and Sassen, K.: The CloudSat mission and the  
968 A-Train: A new dimension of space-based observations of clouds and precipitation, *Bull. Amer. Meteor.*  
969 *Soc.*, 83, 1771-1790, 2002.

970 Stubenrauch, C. J., Rossow, W. B., Kinne, S., Ackerman, S., Cesana, G., Chepfer, H., Di Girolamo, L.,  
971 Getzewich, B., Guignard, A., Heidinger, A., Maddux, B. C., Menzel, W. P., Minnis, P., Pearl, C., Platnick,  
972 S., Poulsen, C., Riedi, J., Sun-Mack, S., Walther, A., Winker, D., Zeng, S., and Zhao, G.: Assessment of  
973 global cloud datasets from satellites: project and database initiated by the GEWEX radiation panel,

974 Bulletin of the American Meteorological Society, 94, 1031-1049, 10.1175/bams-d-12-00117.1, 2013.  
975 Su, T., Zheng, Y., and Li, Z.: Methodology to determine the coupling of continental clouds with surface  
976 and boundary layer height under cloudy conditions from lidar and meteorological data, Atmospheric  
977 Chemistry and Physics, 22, 1453-1466, 10.5194/acp-22-1453-2022, 2022.  
978 Tan, Z., Huo, J., Ma, S., Han, D., Wang, X., Hu, S., and Yan, W.: Estimating cloud base height from  
979 Himawari-8 based on a random forest algorithm, Int J Remote Sens, 42, 2485-2501,  
980 10.1080/01431161.2020.1854891, 2020.  
981 Thorsen, T. J., Fu, Q., and Comstock, J.: Comparison of the CALIPSO satellite and ground-based  
982 observations of cirrus clouds at the ARM TWP sites, Journal of Geophysical Research: Atmospheres,  
983 116, 10.1029/2011jd015970, 2011.  
984 Viúdez-Mora, A., Costa-Surós, M., Calbó, J., and González, J. A.: Modeling atmospheric longwave  
985 radiation at the surface during overcast skies: The role of cloud base height, Journal of Geophysical  
986 Research: Atmospheres, 120, 199-214, 10.1002/2014jd022310, 2015.  
987 Wang, F., Min, M., Xu, N., Liu, C., Wang, Z., and Zhu, L.: Effects of linear calibration errors at low  
988 temperature end of thermal infrared band: Lesson from failures in cloud top property retrieval of  
989 FengYun-4A geostationary satellite, IEEE Transactions on Geoscience and Remote Sensing, 60,  
990 5001511, 10.1109/TGRS.2022.3140348, 2022.  
991 Wang, T., Shi, J., Ma, Y., Letu, H., and Li, X.: All-sky longwave downward radiation from satellite  
992 measurements: General parameterizations based on LST, column water vapor and cloud top  
993 temperature, ISPRS Journal of Photogrammetry and Remote Sensing, 161, 52-60,  
994 10.1016/j.isprsjprs.2020.01.011, 2020.  
995 Wang, X., Min, M., Wang, F., Guo, J., Li, B., and Tang, S.: Intercomparisons of cloud mask product  
996 among Fengyun-4A, Himawari-8 and MODIS, IEEE Transactions on Geoscience and Remote Sensing, 57,  
997 8827-8839, 10.1109/TGRS.2019.2923247 2019.  
998 Wang, Z., Vane, D., Stephens, G., Reinke, D., and TBD: Level 2 combined radar and lidar cloud scenario  
999 classification product process description and interface control document, 2012.  
1000 Warren, S. G. and Eastman, R.: Diurnal Cycles of Cumulus, Cumulonimbus, Stratus, Stratocumulus, and  
1001 Fog from Surface Observations over Land and Ocean, J Climate, 27, 2386-2404,  
1002 10.1175/jcli-d-13-00352.1, 2014.  
1003 Winker, D. M., Vaughan, M. A., Omar, A., Hu, Y., Powell, K. A., Liu, Z., Hunt, W. H., and Young, S. A.:  
1004 Overview of the CALIPSO mission and CALIOP data processing algorithms, J. Atmos. Oceanic. Technol.,  
1005 26, 2310-2323, 10.1175/2009JTECHA1281.1, 2009.  
1006 Yang, J., Li, S., Gong, W., Min, Q., Mao, F., and Pan, Z.: A fast cloud geometrical thickness retrieval  
1007 algorithm for single-layer marine liquid clouds using OCO-2 oxygen A-band measurements, Remote  
1008 Sensing of Environment, 256, 10.1016/j.rse.2021.112305, 2021.  
1009 Young, S. A. and Vaughan, M. A.: The retrieval of profiles of particulate extinction from Cloud Aerosol  
1010 Lidar Infrared Pathfinder Satellite Observations (CALIPSO) data: Algorithm description, J. Atmos.  
1011 Oceanic. Technol., 26, 1105-1119, 10.1175/2008JTECHA1221.1, 2009.  
1012 Zhang, Y., Zhang, L., Guo, J., Feng, J., Cao, L., Wang, Y., Zhou, Q., Li, L., Li, B., Xu, H., Liu, L., An, N., and  
1013 Liu, H.: Climatology of cloud-base height from long-term radiosonde measurements in China,  
1014 Advances in Atmospheric Sciences, 35, 158-168, 10.1007/s00376-017-7096-0, 2018.  
1015 Zheng, Y. and Rosenfeld, D.: Linear relation between convective cloud base height and updrafts and  
1016 application to satellite retrievals, Geophys Res Lett, 42, 6485-6491, 10.1002/2015gl064809, 2015.  
1017 Zheng, Y., Sakradzija, M., Lee, S.-S., and Li, Z.: Theoretical Understanding of the Linear Relationship

1018 between Convective Updrafts and Cloud-Base Height for Shallow Cumulus Clouds. Part II: Continental  
1019 Conditions, *J Atmos Sci*, 77, 1313-1328, 10.1175/jas-d-19-0301.1, 2020.

1020 Zhou, Q., Zhang, Y., Li, B., Li, L., Feng, J., Jia, S., Lv, S., Tao, F., and Guo, J.: Cloud-base and cloud-top  
1021 heights determined from a ground-based cloud radar in Beijing, China, *Atmospheric Environment*, 201,  
1022 381-390, 10.1016/j.atmosenv.2019.01.012, 2019.

1023 Zhou, R., Pan, X., Xiaohu, Z., Na, X., and Min, M.: Research progress and prospects of atmospheric  
1024 motion vector based on meteorological satelliteimages, *Reviews of Geophysics and Planetary Physics*  
1025 (In Chinese), 55, 184-194, 10.19975/j.dqyx.2022-077, 2024.

1026 Zhu, Y., Rosenfeld, D., Yu, X., Liu, G., Dai, J., and Xu, X.: Satellite retrieval of convective cloud base  
1027 temperature based on the NPP/VIIRS Imager, *Geophys Res Lett*, 41, 1308-1313,  
1028 10.1002/2013gl058970, 2014.

1029  
1030  
1031  
1032  
1033  
1034  
1035  
1036  
1037  
1038  
1039  
1040  
1041  
1042  
1043  
1044  
1045  
1046  
1047  
1048  
1049  
1050  
1051  
1052  
1053

1054  
1055  
1056  
1057  
1058  
1059

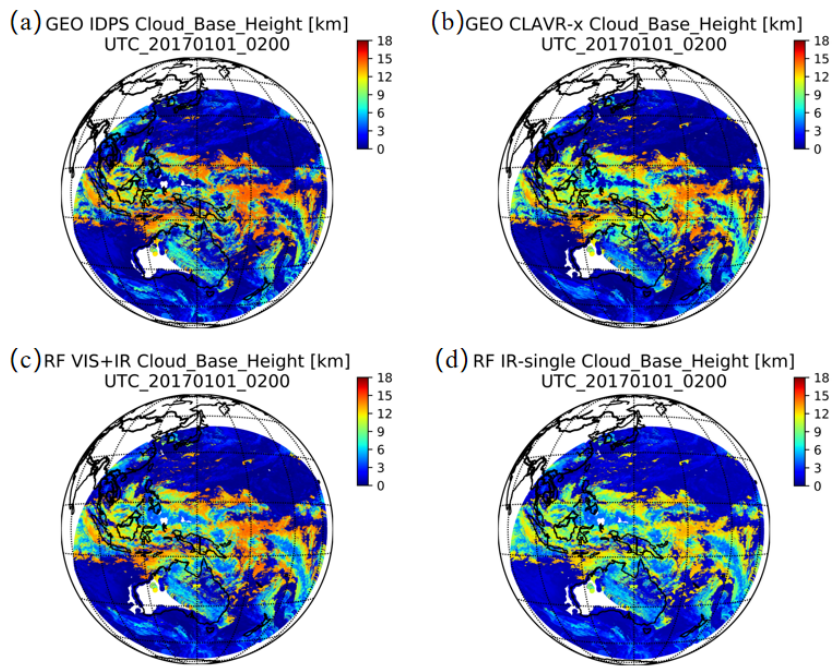
**Tables and Figures**

**Table 1.** Predictand and predictor variables for both visible (VIS)+infrared (IR) model and IR-single regression model training, which are divided according to the different predictor variables from satellite and NWP data

Predictand	IR-single model input	VIS+IR model input
<b>Predictor [satellite measurements]</b>	BT(3.9 $\mu$ m), BT(6.2 $\mu$ m), BT(6.9 $\mu$ m), BT(7.3 $\mu$ m), BT(8.6 $\mu$ m), BT(9.6 $\mu$ m), BT(10.4 $\mu$ m), BT(11.2 $\mu$ m), BT(12.4 $\mu$ m), BT(13.3 $\mu$ m), BTD(11.2–12.4 $\mu$ m), BTD(11.2– 13.3 $\mu$ m) [Unit = K], Air Mass (1/cos(VZA)), View azimuth angles [Unit = degree], Cloud top height from H8/AHI [unit: m], Cloud top temperature from H8/AHI [unit: K]	BT(3.9 $\mu$ m), BT(6.2 $\mu$ m), BT(6.9 $\mu$ m), BT(7.3 $\mu$ m), BT(8.6 $\mu$ m), BT(9.6 $\mu$ m), BT(10.4 $\mu$ m), BT(11.2 $\mu$ m), BT(12.4 $\mu$ m), BT(13.3 $\mu$ m), BTD(11.2–12.4 $\mu$ m), BTD(11.2– 13.3 $\mu$ m) [Unit = K], Air Mass(1/cos(VZA)), Air Mass(1/cos(SZA)), View/Solar Azimuth angles [Unit = degree], Cloud top height from H8/AHI [unit: m], Cloud top temperature from H8/AHI [unit: K] Ref(0.47 $\mu$ m), Ref(0.51 $\mu$ m), Ref(0.64 $\mu$ m), Ref(0.86 $\mu$ m), Ref(1.64 $\mu$ m), Ref(2.25 $\mu$ m)
<b>Predictor [GFS NWP]</b>	Altitude profile (from surface to about 21 km, 67 layers) [unit: m], Temperature profile (from surface to about 21 km, 67 layers) [unit: K], Relative humidity profile (from surface to about 21 km, 67 layers) [unit: %], Total precipitable water, Surface temperature [unit: K]	Altitude profile (from surface to about 21 km, 67 layers) [unit: m], Temperature profile (from surface to about 21 km, 67 layers) [unit: K], Relative humidity profile (from surface to about 21 km, 67 layers) [unit: %], Total precipitable water, Surface temperature [unit: K]
<b>Predictor [other]</b>	Surface elevation [unit: m]	Surface elevation [unit: m]

1060 Notes: VZA = view zenith angle [unit: degree]; SZA = solar zenith angle [unit:  
1061 degree]  
1062  
1063  
1064

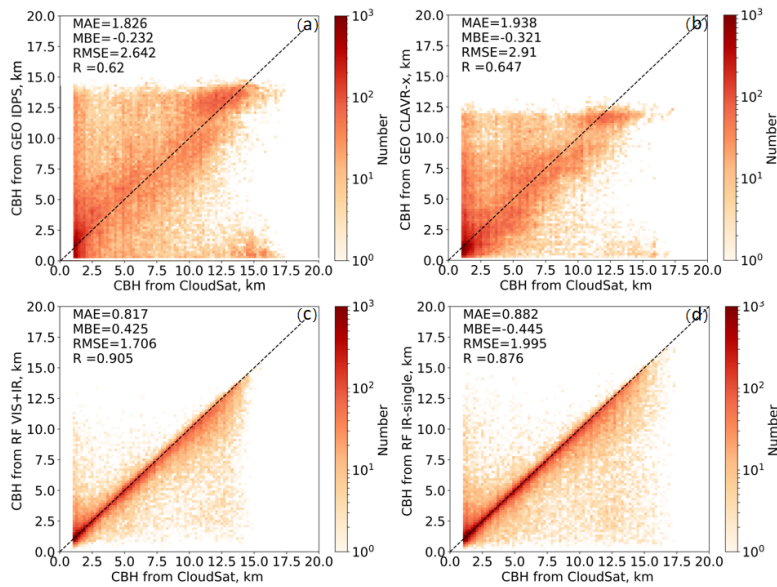
1065  
1066  
1067  
1068  
1069  
1070  
1071  
1072  
1073  
1074



1075  
1076 **Figure 1.** Comparison of full disk CBH results retrieved by the four independent  
1077 algorithms at 02:00 UTC on January 1, 2017. (a) GEO IDPS algorithm, (b) GEO  
1078 Clouds from AVHRR Extended (CLAVR-x) algorithm, (c) ML-based (RF, random  
1079 forest) VIS+IR algorithm and (d) ML-based (RF) IR-single algorithm.

1080  
1081  
1082  
1083  
1084  
1085  
1086

1087  
1088  
1089  
1090

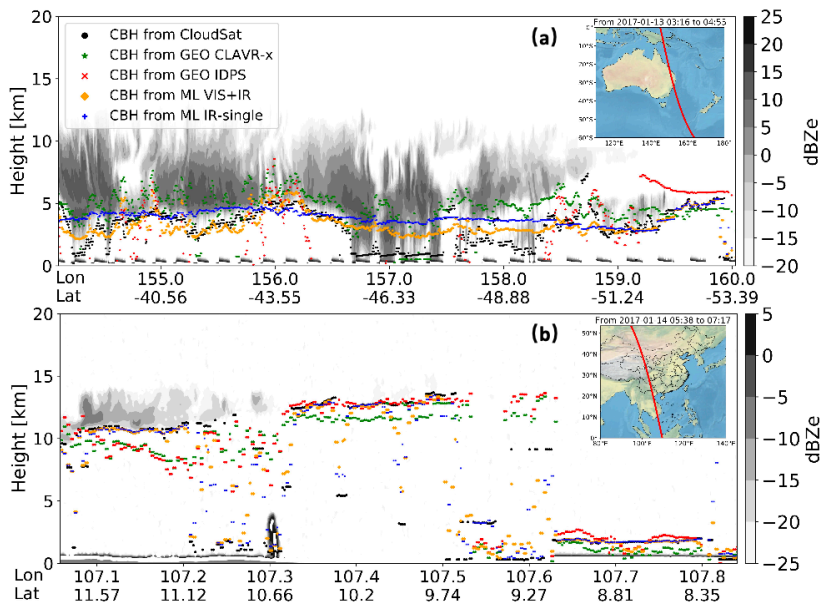


1091 **Figure 2.** Density distributions of CBHs retrieved from (a) GEO IDPS, (b) GEO  
1092 CLAVR-x, (c) VIS+IR and (d) IR-single algorithms compared with the CBHs from  
1093 the joint CloudSat/CALIPSO product (taken as true values) in 2017 for both single  
1094 and multilayer clouds. The mean absolute error (MAE), mean bias error (MBE), root  
1095 mean square error (RMSE) and R are listed in each subfigure where the difference  
1096 exceeds the 95% significance level ( $p < 0.05$ ) according to the Pearson's  $\chi^2$  test.  
1097

1098  
1099  
1100  
1101  
1102  
1103  
1104  
1105  
1106



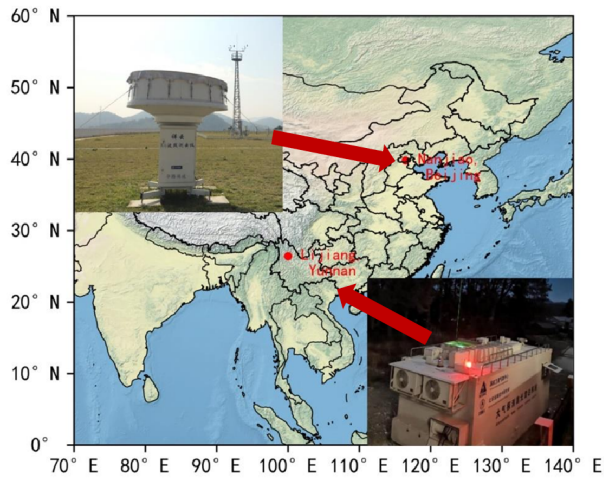
1107  
1108  
1109  
1110  
1111



1112 **Figure 3.** Inter-comparisons of CBH products retrieved by CloudSat (red solid circle),  
1113 the GEO IDPS algorithm (blue solid circle), the GEO CLAVR-x (green solid circle),  
1114 the ML-based VIS+IR model algorithm (orange solid circle), and the ML-based  
1115 IR-single model algorithm (pink solid circle) at (a) 03:16–04:55 UTC on January 13,  
1116 2017 (a) and (b) 05:38–07:17 UTC on January 14, 2017. The black and gray colormap  
1117 represents the matched CloudSat radar reflectivity.  
1118

1119  
1120  
1121  
1122  
1123  
1124  
1125

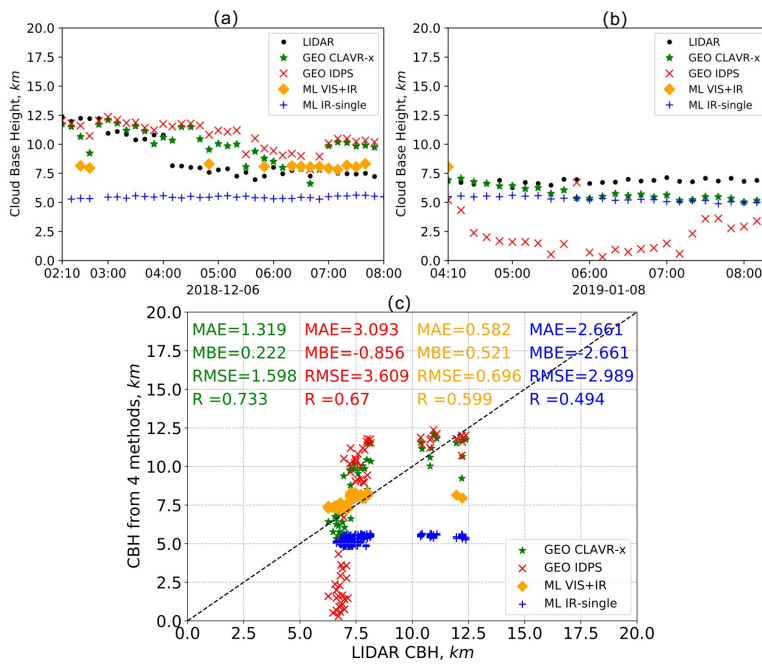
1126  
1127  
1128  
1129  
1130  
1131



1132  
1133 **Figure 4.** Geographical locations and photos of lidar and cloud radar at Yunnan  
1134 Lijiang and Beijing Nanjiao stations.

1135  
1136  
1137  
1138  
1139  
1140  
1141  
1142  
1143  
1144  
1145  
1146  
1147  
1148

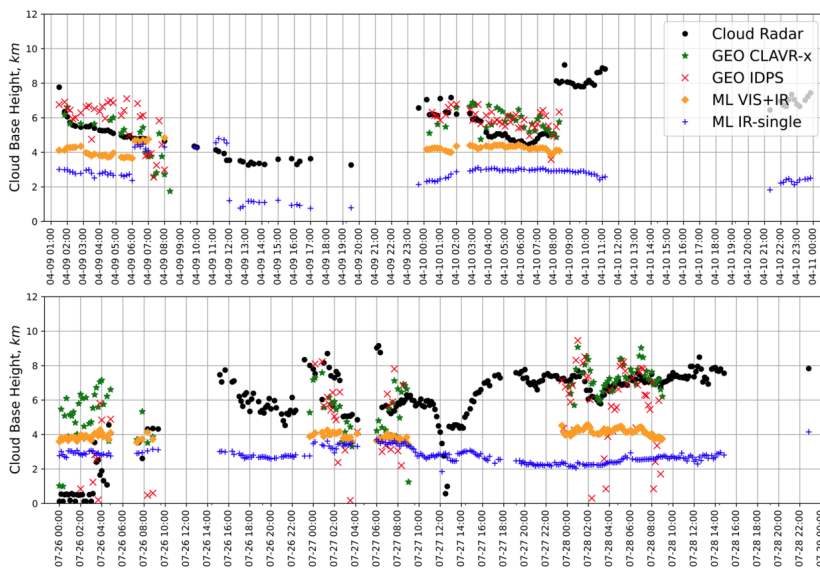
1149  
 1150  
 1151  
 1152  
 1153



1154  
 1155 **Figure 5.** Comparisons of the CBHs from the ground-based lidar measurements  
 1156 (black solid circle) at Yunnan Lijiang station and the four GEO satellite retrieval  
 1157 algorithms, namely the GEO IDPS (red cross symbol), the GEO CLAVR-x (green  
 1158 solid asterisk), the ML-based VIS+IR model (orange solid diamond) and the  
 1159 ML-based IR-single model (blue plus sign) algorithms. Figure 5a and 5b show the  
 1160 time series of CBHs from lidar and the four GEO satellite retrieval algorithms on  
 1161 December 6, 2018 and January 8, 2019, respectively. Fig 5c shows the scatterplots of  
 1162 CBH samples from the lidar measurements and the four retrieval algorithms.

1163  
 1164  
 1165

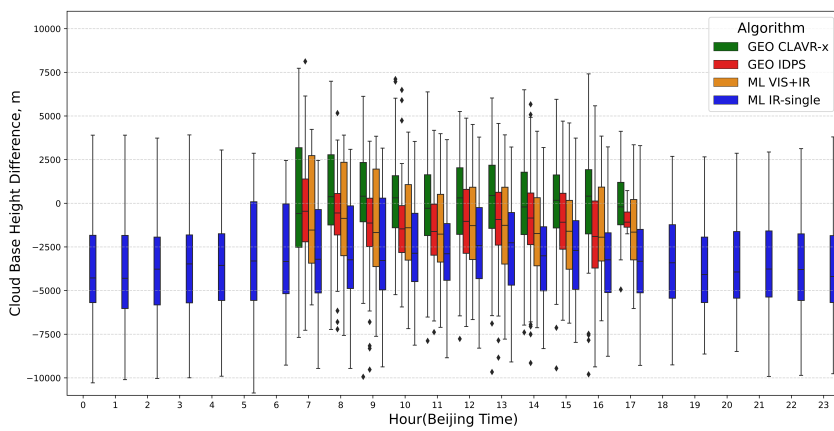
1166  
1167  
1168  
1169  
1170  
1171



1172  
1173  
1174  
1175  
1176  
1177  
1178  
1179  
1180  
1181  
1182  
1183  
1184

**Figure 6.** Same as Figure 5, but for the CBH sample results from the cloud radar at Beijing Nanjiao station (black solid circle) on April 9–10, 2017 (top panel) and July 26–28, 2017 (bottom panel).

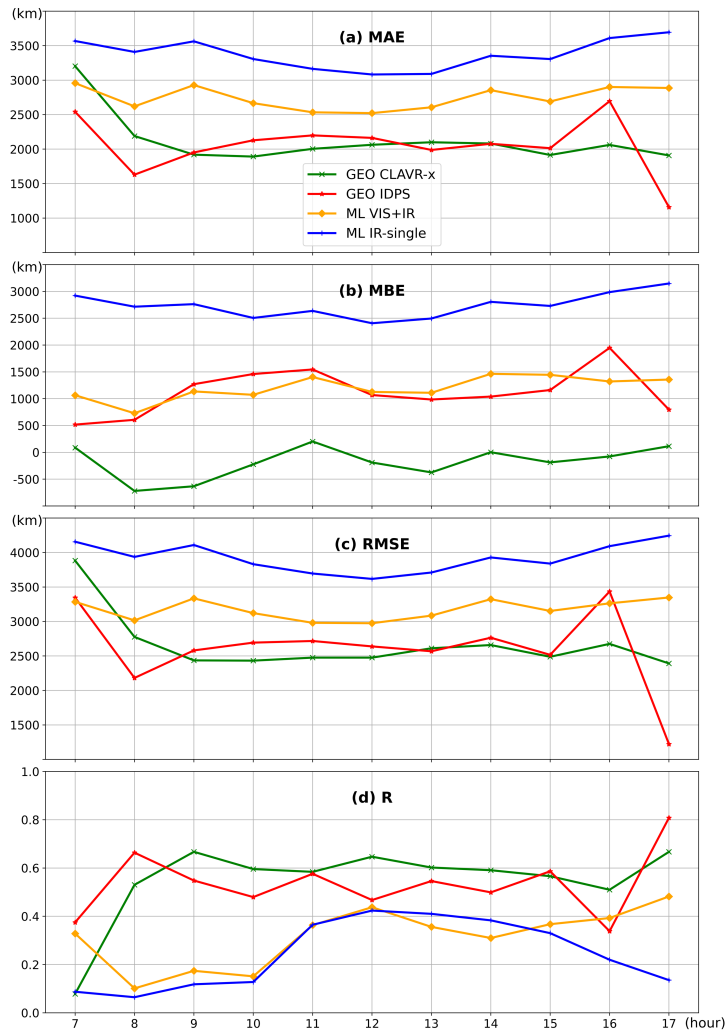
1185  
1186  
1187  
1188  
1189  
1190  
1191  
1192



1193  
1194 **Figure 7.** Box plots of the hourly CBH errors of four GEO satellite retrieval  
1195 algorithms (GEO IDPS, GEO CLAVR-x, ML-based VIS+IR and ML-based IR-single)  
1196 relative to the CBHs from the cloud radar at Beijing Nanjiao station in 2017. The box  
1197 symbols signify the 25th, 50th and 75th percentiles of errors. The most extreme  
1198 sample points between the 75th and outlier, and the 25th percentiles and outliers are  
1199 marked as whiskers and diamonds, respectively. Except for the period between 7 and  
1200 17 (local time), the three algorithms of GEO CLAVR-x, GEO IDPS, and ML VIS+IR  
1201 are unavailable due to the lack of reflected solar radiance measurements.

1202  
1203  
1204  
1205  
1206  
1207  
1208  
1209  
1210

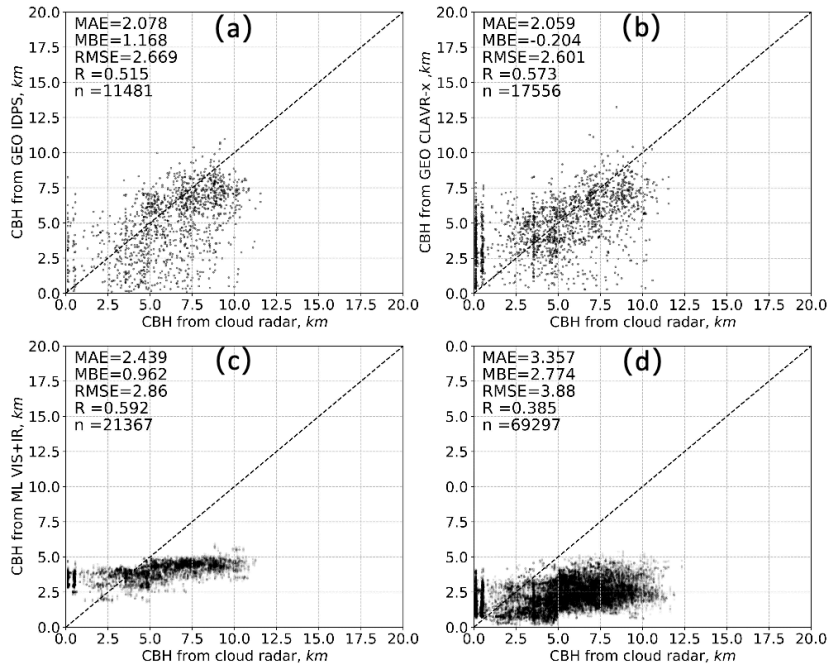
1211  
1212



1213  
1214 **Figure 8.** Comparisons of hourly (a) MAE, (b) MBE, (c) RMSE, and (d) R of CBH  
1215 (relative to the CBHs from the cloud radar at Beijing Nanjiao station) from 07 to 17  
1216 (local time) between four retrieval algorithms (GEO IDPS, GEO CLAVR-x,  
1217 ML-based VIS+IR and ML-based IR-single) in 2017.

1218  
1219

1220  
1221



1222  
1223  
1224  
1225  
1226  
1227  
1228  
1229  
1230  
1231

**Figure 9.** Comparisons between the CBHs from the cloud radar at Beijing Nanjiao station and the matched CBHs from the four retrieval algorithms (GEO IDPS, GEO CLAVR-x, ML-based VIS+IR and ML-based IR-single) in 2017.